Infinite horizon billiards: Transport at the border between Gauss and Lévy universality classes

Lior Zarfaty [1,*] Alexander Peletskyi,[2] Eli Barkai,[1] and Sergey Denisov[3]

[1]*Department of Physics, Institute of Nanotechnology and Advanced Materials, Bar-Ilan University, Ramat-Gan 52900, Israel*
[2]*Institute of Physics, University of Augsburg, Universitätsstrasse 1, 86135 Augsburg, Germany*
[3]*Department of Computer Science, Oslo Metropolitan University, 0130 Oslo, Norway*

We consider transport in two billiard models, the infinite horizon Lorentz gas and the stadium channel, presenting analytical results for the spreading packet of particles. We first obtain the cumulative distribution function of traveling times between collisions, which exhibits nonanalytical behavior. Using a renewal assumption and the Lévy walk model, we obtain the particles' probability density. For the Lorentz gas, it shows a distinguished difference when compared with the known Gaussian propagator, as the latter is valid only for extremely long times. In particular, we show plumes of particles spreading along the infinite corridors, creating power-law tails of the density. We demonstrate the slow convergence rate via summation of independent and identically distributed random variables on the border between Lévy and Gauss laws. The renewal assumption works well for the Lorentz gas with intermediate-size scattering centers, but fails for the stadium channel due to strong temporal correlations. Our analytical results are supported with numerical samplings.

I. INTRODUCTION

The infinite horizon Lorentz gas [1] is a paradigmatic model of deterministic classical transport, thoroughly studied by physicists [2–8] and mathematicians [9–22]. It consists of an infinite periodic lattice of convex obstacles, and pointlike particles which undergo elastic collisions with them. The most common configuration of the Lorentz gas model is composed of circular scatterers arranged into an infinite square lattice of unit spacing. Several important properties of this model, such as ergodicity [14] and algebraic decay of the velocity correlations in time [11], have been rigorously proven. Importantly, Bleher [12] showed that a particle's position vector $r(t)$ has a limiting Gaussian distribution when normalized correctly. More accurately, the quantity $\lim_{t\to\infty}[r(t) - r(0)]/\sqrt{t \ln(t)}$ is a two-dimensional Gaussian variable with zero mean and a covariance matrix which depends on the arrangement of scatterers. However, this asymptotic form is valid only when $\ln[\ln(N)]/\ln(N) = \epsilon \ll 1$, where N is the number of collisions. To satisfy this condition, N has to be extremely large (e.g., $\epsilon = 0.01$ requires that $N \approx 10^{281}$). Bleher's time is too large to be physically relevant [3], while microscopic intercollision times cannot describe transport processes happening on much larger timescales. As such, key features of the Lorentz gas model can only be seen for intermediate times that are most relevant for transport regimes. Unfortunately, currently there are no analytical results for these *mesoscopic* times.

In billiard models, an important characteristic of the transport is the presence (or absence) of infinite horizons, corridors along which collisionless ballistic trajectories propagate (see Fig. 1). The packet of spreading particles in an *infinite horizon* billiard model exhibits two main features: The center part of the packet is approximately Gaussian and the far tails are described by plumes of particles spreading along the infinite corridors. For a specific configuration of the Lorentz gas, we found in our previous Rapid Communication [23] that the scatterers' geometry is embedded in the crosslike shape of the spreading packet [see Figs. 1(a) and 2]. Here we wish to extend our theory to other configurations, showing its generality. For this aim, we consider the Lorentz gas with corridors forming a British flaglike structure for the packet of spreading particles [seen in Figs. 1(b) and 3], together with a quasi-one-dimensional transport in a chain of concatenated Bunimovich billiard stadiums [3,9] [seen in Figs. 1(c) and 4]. While the models are distinctive, along the corridors the far tails of the density decay spatially with a universal power law, a feature well described by the Lévy walk model [24–27].

Our analysis is composed of two main ingredients; one of them is obtaining the aforementioned billiard systems' full distribution of intercollision times. For the Lorentz gas, results in the limits of $R \to 1/2$ and $\tau \to \infty$ (where R is a scatterer's radius and τ is an intercollision time) were found by Bouchaud and Le Doussal [2]. More recently, an asymptotic form in the limit of $R \to 0$ was established [13,15,19]. However, this important aspect in the characterization of transport is hardly discussed in the literature when finite-size scatterers are considered. This distribution's probability density function (PDF) exhibits a far tail obeying

$$\lim_{\tau \to \infty} \tau^3 \psi(\tau) = \tau_0^2, \tag{1}$$

which is valid for both limits of large and small scatterers. Therefore, we use a Lévy walk model with exponent -3 for the other ingredient, which is calculating the density of spreading particles. A principal issue here is that in a Lévy walk approximation one uses a renewal assumption, i.e., one neglects correlations between consecutive collisions. It was
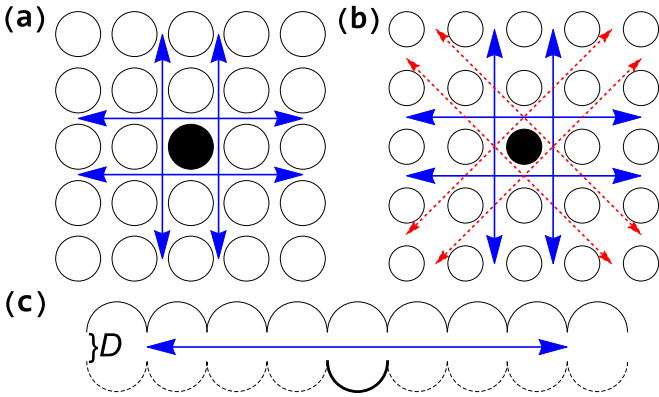
---
*lior.zarfaty@mail.huji.ac.il

FIG. 1. The considered models: the infinite horizon Lorentz gas with (a) two and (b) four open horizons and (c) the stadium channel model. For the Lorentz gas we take the lattice constant to be 1, while for the stadium channel we use 1 for the radius of a semicircle wall. The parameter which controls the qualitative behavior for the Lorentz gas is the scatterers' radius R. When $1/\sqrt{8} \leqslant R < 1/2$, there are two directions of infinite corridors. A particle that collided with the black circle can fly along the blue solid arrows, reaching scatterers along them. Decreasing the radius such that $1/\sqrt{20} \leqslant R < 1/\sqrt{8}$ creates two additional directions of infinite corridors. A particle that collided with the black circle can now fly along the red dashed arrows as well (see Fig. 7 for additional details). In the stadium channel model the controlling parameter is the walls' separation $D > 0$. A particle which was scattered from the thick bottom semicircle can reach any stadium of the top row, but can also hit the origin semicircle again (the dashed stadiums are unreachable in this case). All of the numerical simulations were performed using unit speed, namely, $V = 1$.

shown that for the crosslike configuration of the Lorentz gas and in the limit of large scattering centers, this condition is nullified as an effective trapping mechanism emerges [4]. In contrast, when the scattering centers are not too large, the Lévy walk with the obtained cumulative distribution function (CDF) of the waiting times works perfectly, as demonstrated below. Deviations from the renewal theory do exist for the stadium channel model where correlations are strong, as we show below. However, this does not imply that the Lévy walk model is not predictive here as well, and in fact we find the opposite. Another primary issue is caused since these two systems are operating on the border between Gauss and

Lévy central limit theorems, due to the exponent -3, which causes a logarithmic divergence of $\psi(\tau)$'s second moment. Thus, an ultraslow convergence rate problem arises that can be understood via a toy model: summation of independent and identically distributed (IID) random variables (RVs), with a common symmetric PDF that decays algebraically with a power of -3 for a large argument. Here we encounter the same type of convergence problem discussed in the first paragraph, which is neutralized using what we call the Lambert scaling approach. This is a crucial step for these systems, as it allows us to compare finite-time simulations with our theory for duration regimes where previous results do not hold.

The rest of this paper is organized as follows. In Sec. II we provide an example of the Lambert scaling for sums of IID RVs. In Sec. III we derive the main formula of the spatial PDFs by using the Lévy walk model. In Sec. IV we obtain the CDFs of intercollision times for the Lorentz gas and stadium channel. We discuss our results in Sec. V.

II. SIMPLIFIED CASE OF LAMBERT SCALING

We now consider the problem of summation of IID RVs, drawn from a power-law distribution. We work at the border between Gauss and Lévy central limit theorems, which is clearly related to the exponent -3 in Eq. (1). Some aspects of this by far simpler approach are important for the discussed billiard models. In particular, at this transition we find a critical slowing down in the sense that convergence to the Gaussian limit theorem is ultraslow [28], a problem which is resolved by Lambert scaling. Consider a sum of $N \gg 1$ IID RVs

$$x = \sum_{n=1}^{N} \chi_n, \tag{2}$$

where the summands are drawn from a common symmetric PDF which obeys $f(\chi \to \infty) \simeq \chi_0^2/\chi^3$. We define the scaled sum as $\bar{x} = x/\sqrt{\chi_0^2 N \Omega(N)/2}$, with $N\Omega(N)$ a scaling parameter, soon to be determined. We use the characteristic function

$$\langle \exp(i\bar{k}\bar{x}) \rangle = \exp\left\{ N \ln\left[\tilde{f}\left(\frac{\bar{k}}{\sqrt{\chi_0^2 N \Omega(N)/2}} \right) \right] \right\}, \tag{3}$$

where $\tilde{f}(k)$ is the Fourier transform of $f(\chi)$. Assuming that $\Omega(N)$ monotonically increases with N, the small-k behavior
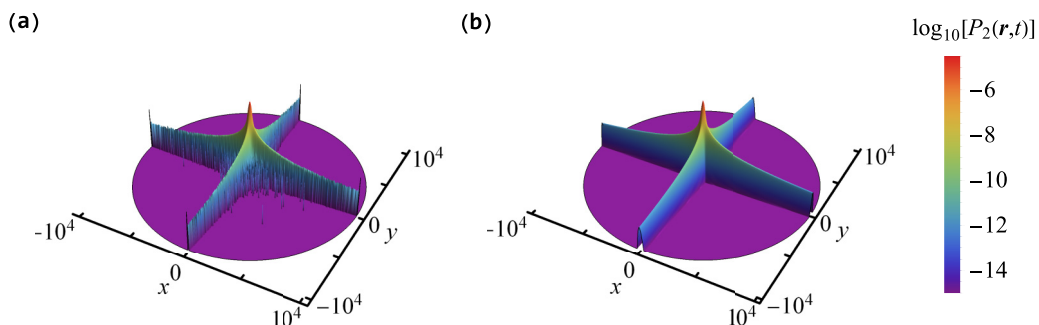

FIG. 2. The position's probability density function for the Lorentz gas with two open horizons produces a crosslike geometry. Here the lattice constant and speed are 1, the scatterers' radius is $R = 0.4$, and the time duration is $t = 10^4$. (a) The Lorentz gas simulation has approximately 10^9 sampled trajectories. (b) Our theory Eq. (26) with $q = 0$ reproduces the simulation well.
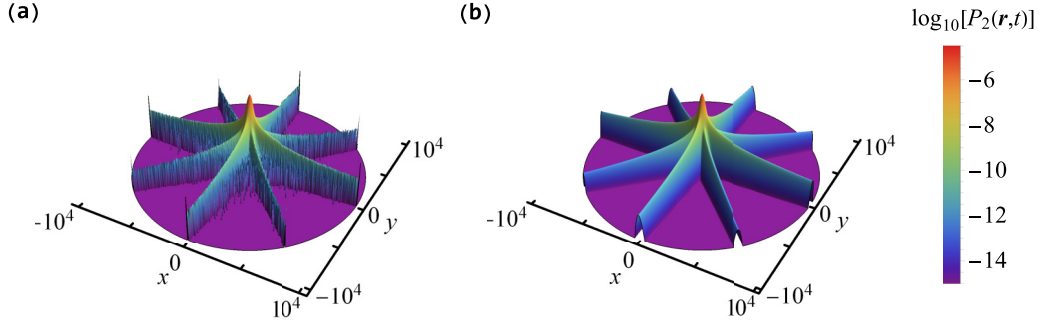
FIG. 3. The position's probability density function for the Lorentz gas with four open horizons produces a British flaglike shape. Here the lattice constant and speed are 1, the scatterers' radius is $R = 0.3$, and the time duration is $t = 10^4$. The (a) Lorentz gas simulation is reproduced without any fitting by (b) our theory, which is given by Eqs. (26) and (47).

of $\tilde{f}(k)$ is considered,

$$\tilde{f}(k) \simeq 1 + \tfrac{1}{2}(\chi_0 k)^2 \ln[(C_f \chi_0 k)^2], \quad (4)$$

which is derived in Appendix A. The first term is the normalization, while the second is related to the power-law
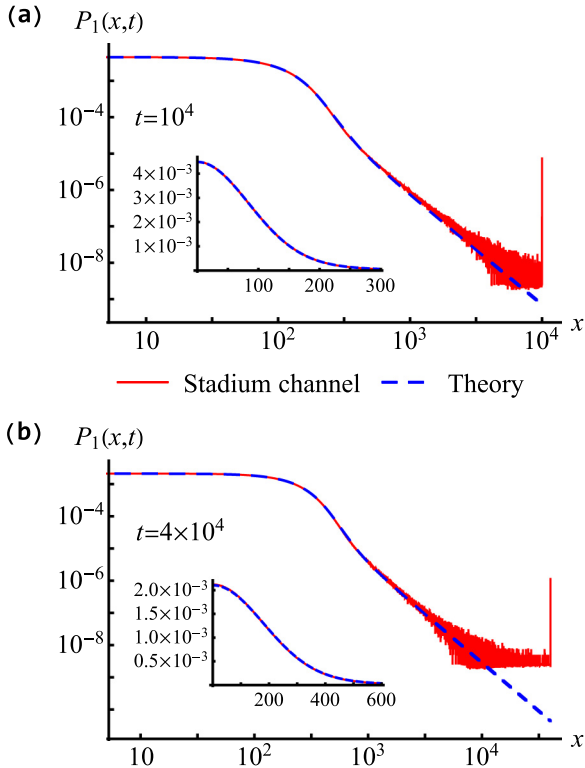

FIG. 4. The position's probability density function for the stadium channel model with (a) $t = 10^4$ and (b) $t = 4 \times 10^4$, where $D = 1$. The solid red line is the stadium channel numerical simulations and the dashed blue line is Eq. (23). Using a two-parameter fitting procedure and the simulation of duration $t = 10^4$, we find that $C_\psi^2 \langle \tau \rangle \approx 0.3776$ and $\langle \tau \rangle / \tau_0^2 \approx 7.0607$. These values were used when calculating $P_1(x, t)$ for $t = 4 \times 10^4$. The curves match well, which means that Eq. (23) can indeed describe the stadium channel model, given an effective waiting-time distribution. The stadium channel simulations have around 2×10^8 sampled trajectories (the smallest values in the histograms represent cells with a single event).

tail of $f(\chi)$, with C_f being

$$C_f = \exp\left\{\gamma - \frac{3}{2} - \int_0^{\chi_0} d\chi \, f(\chi)\left(\frac{\chi}{\chi_0}\right)^2 \right.$$

$$\left. - \int_{\chi_0}^{\infty} d\chi \left[f(\chi)\left(\frac{\chi}{\chi_0}\right)^2 - \frac{1}{\chi} \right]\right\}, \quad (5)$$

where $\gamma \approx 0.5772$ is Euler's constant. Inserting Eq. (4) into Eq. (3) and expanding, we get

$$\langle \exp(i\bar{k}\bar{x}) \rangle \simeq \exp\left\{ \frac{\bar{k}^2}{\Omega(N)} \ln\left[\frac{2C_f^2 \bar{k}^2}{N\Omega(N)} \right]\right\}. \quad (6)$$

We now determine the slowly increasing function $\Omega(N)$ with the choice

$$\ln\left[\frac{N\Omega(N)}{2C_f^2} \right] = \Omega(N), \quad (7)$$

which yields

$$\Omega(N) = \left| W_{-1}\left(-\frac{2C_f^2}{N} \right) \right|. \quad (8)$$

Here $W_{-1}(\eta)$ is the secondary branch of the Lambert W function [29], defined for $\eta \in [-1/e, 0)$ by the identity $W_{-1}(\eta) = \ln[\eta / W_{-1}(\eta)]$. The Lambert function has the expansion, as $\eta \to 0^-$,

$$|W_{-1}(\eta)| = L_1 + L_2 + \frac{L_2}{L_1} + O\left(\frac{L_2^2}{L_1^2} \right), \quad (9)$$

where $L_1 = \ln(1/|\eta|)$ and $L_2 = \ln[\ln(1/|\eta|)]$. Equations (8) and (9) yield $N\Omega(N) \simeq N \ln(N)$ when $N \to \infty$, reproducing the well-known Gnedenko-Kolmogorov scaling $\sqrt{N \ln(N)}$ [30]. However, for this to be of relevance, one must demand $\ln(N) \gg \ln[\ln(N)]$, which makes the convergence to this mathematical limit ultraslow. Our Lambert scaling approach unites all of the N-dependent logarithmic terms into a single function, thus resolving this problem. We therefore expand Eq. (6) for large $\Omega(N)$, keeping terms up to subleading order during the calculation

$$\langle \exp(i\bar{k}\bar{x}) \rangle \simeq e^{-\bar{k}^2}\left[1 + \frac{\bar{k}^2}{\Omega(N)} \ln(\bar{k}^2) \right]. \quad (10)$$
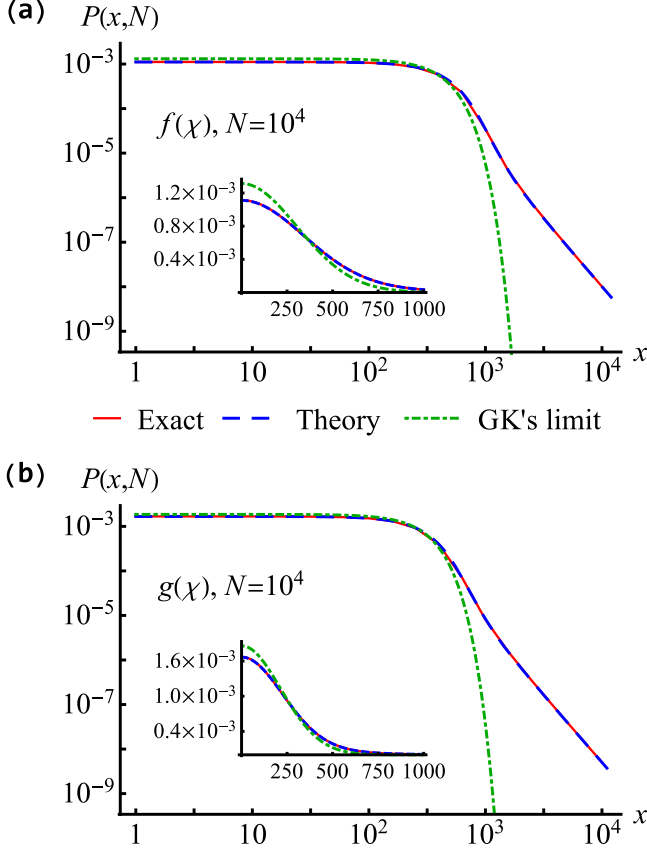
FIG. 5. The probability density function of the sum (2) with $N = 10^4$, and its corresponding Lambert scaling approximation (11). The common PDFs used here are (a) $f(\chi) = 1/|\chi|^3$ when $|\chi| \geqslant 1$ and 0 otherwise and (b) $g(\chi) = (1 + \chi^2)^{-3/2}/2$. The exact values (solid lines) are obtained from an inverse Fourier transform of $\tilde{f}^N(k)$, dashed lines are the theory (11), and dot-dashed lines are the limit distributions of Gnedenko and Kolmogorov (GK) [30].

Inverting Eq. (10) back to position space, we reach our first result, the PDF of x,

$$
P(x, N) \simeq \frac{1}{\sqrt{\pi \xi^2(N)}} \exp\left(-\frac{x^2}{\xi^2(N)}\right)
$$
$$
\times \left\{ 1 + \frac{1}{\Omega(N)} \left[[2 - \gamma - \ln(4)]\left(\frac{1}{2} - \frac{x^2}{\xi^2(N)}\right) \right.\right.
$$
$$
\left.\left. - \frac{1}{2} M^{(1,0,0)}\left(-1; \frac{1}{2}; \frac{x^2}{\xi^2(N)}\right) \right] \right\}, \quad (11)
$$

with $\xi(N) = \sqrt{2\chi_0^2 N \Omega(N)}$. Here $M(\cdots)$ is Kummer's confluent hypergeometric function [29] and the superscript over M denotes its derivative with respect to its first argument. Figure 5 shows a good match between Eq. (11) and the PDF of the sum (2) for two different common density functions $f(\chi)$ and $g(\chi)$, which are defined in the caption, with $N = 10^4$. The Kummer function behaves asymptotically as $M^{(1,0,0)}(-1, 1/2, \eta^2) \simeq -\sqrt{\pi} \exp(\eta^2)/\eta^3$, suggesting that $P(x, N) \simeq N\chi_0^2/x^3$. Thus, the PDF of the sum x reproduces the same power-law tails as of the original common PDF $f(\chi)$. As the distribution of traveling times between collisions

(1) exhibit the same heavy-tail exponent of -3, our next step is implementing Lambert scaling to the Lévy walk model.

III. LAMBERT SCALING OF THE LÉVY WALK MODEL

The d-dimensional Lévy walk model [25,27] is defined as follows. A random walker is placed at $r(0)$ on time $t = 0$. Its movement consists of segments of ballistic motion with constant velocity, separated by collisionlike events which induce a change in the velocity's magnitude and/or direction. The process lasts for a fixed duration, which is the measurement time t. The model employs two PDFs in order to determine the displacement during each of the ballistic motion epochs. The velocity of each segment is drawn from a PDF $F_d(v)$, whose moments are all finite, and is further assumed to be symmetric with respect to each of the components v_j where $1 \leqslant j \leqslant d$ (such that its odd moments vanish). The time duration of each ballistic section is drawn from a PDF $\psi(\tau)$. The movement continues until the allotted measurement time is met; thus the number of collisions N in $[0, t]$ is random. This yields the total displacement as

$$
r(t) - r(0) = \sum_{n=1}^{N} v_{n-1}\tau_n + v_N \tau_b, \quad (12)
$$

where τ_n is the traveling time of the nth walking epoch, v_n is the velocity after the nth collision, and the initial conditions $r(0)$ and v_0 are randomly chosen. The traveling times and velocities $\{\tau_n, v_n\}$ (with $1 \leqslant n \leqslant N$) are IID RVs, with the last movement duration being $\tau_b = t - \sum_{n=1}^{N} \tau_n$. Notice that the measurement time divided by the mean time between collisions $t/\langle \tau \rangle$ and the lengths of intercollision travel $\{v_{n-1}\tau_n\}$ roughly correspond to N and $\{\chi_n\}$ from the preceding section, respectively. We denote the particle's speed by V, which is kept unchanged in the billiards systems due to the collisions' elasticity (in the numerical simulations $V = 1$). Let us denote the probability to find the walker at position r on time t by $P_d(r, t)$ and let $\Pi_d(k, u)$ be its Fourier and Laplace transform

$$
\Pi_d(k, u) = \int d^d r \int_0^\infty dt \, P_d(r, t) e^{-ut + ik \cdot x}. \quad (13)
$$

An exact expression of $\Pi_d(k, u)$ is given by the Montroll-Weiss equation [31]

$$
\Pi_d(k, u) = \left\langle \frac{1 - \hat{\psi}(u - ik \cdot v)}{u - ik \cdot v} \right\rangle \frac{1}{1 - \langle \hat{\psi}(u - ik \cdot v) \rangle}, \quad (14)
$$

where $\hat{\psi}(u)$ is the Laplace transform of $\psi(\tau)$, defined as

$$
\hat{\psi}(u) = \int_0^\infty d\tau \, \psi(\tau) e^{-u\tau}, \quad (15)
$$

and

$$
\langle \cdots \rangle = \int d^d v \cdots F_d(v), \quad (16)
$$

with the above integral carried over all velocity space.

We now direct the reader's attention to two points before advancing with the calculation. First, note that the assumption of finite moments for the velocity distribution $F_d(v)$ is crucial to our theory. For example, a diverging second moment yields Lévy statistics in the bulk instead of a Gaussian, whereas for

the Lorentz gas it is rigorously proven to be the latter case [12]. Second, in Ref. [27] the authors discuss two different variations of the Lévy walk: the velocity model and the jump model. For the former, particles move constantly until the measurement time ends, their last traveling epoch being τ_b. However, for the latter particles are missing this final segment of walk. Therefore, the two models differ only when considering approximation theories of the far tail (under the condition of finite mean time between collisions). As our theory is intended to approximate the bulk of the PDF $P_d(\mathbf{r}, t)$, these two aforementioned cases are indistinguishable. Technically speaking, this difference is manifested by a different numerator of Eq. (14), which does not change its approximated versions which appear below [Eqs. (20) and (25)]. Further, in the Lorentz gas a particle's velocity is unity at any moment of travel; therefore the velocity model is more suitable if compared to the jump model.

To approximate Eq. (14) we use the asymptotic behavior of $\psi(\tau)$ [Eq. (1)], which implies that for small u,

$$\hat{\psi}(u) \simeq 1 - \langle\tau\rangle u - \frac{1}{2}(\tau_0 u)^2 \ln(C_\psi \tau_0 u), \qquad (17)$$

which is derived in Appendix B. Here the first term is the normalization, $\langle\tau\rangle$ is the mean time between collisions, and the last term is related to the power-law tail of $\psi(\tau)$, with C_ψ being

$$C_\psi = \exp\left\{\gamma - \frac{3}{2} - \int_0^{\tau_0} d\tau \, \psi(\tau)\left(\frac{\tau}{\tau_0}\right)^2 \right.$$
$$\left. - \int_{\tau_0}^\infty d\tau \left[\psi(\tau)\left(\frac{\tau}{\tau_0}\right)^2 - \frac{1}{\tau}\right]\right\}. \qquad (18)$$

We assume a scaling of $u \sim k^2 L(k)$, where $L(\cdots)$ is some logarithmiclike function and $k = |\mathbf{k}|$. This suggests that $u \ll k$ when $k \to 0$, and as such we can expand the Montroll-Weiss equation (14) in the small parameter u/kv, where $v = |\mathbf{v}|$ (see Appendix C). For the one-dimensional stadium channel model, we apply the distribution of velocities

$$F_1(v_x) = \frac{1}{2}[\delta(v_x - V) + \delta(v_x + V)], \qquad (19)$$

where $\delta(\cdots)$ is Dirac's delta function, and in our case $V = 1$. We obtain in Appendix C the Fourier expansion for the distribution

$$\tilde{P}_1(\kappa_x, t) \simeq \frac{2e^{-\kappa_x^2}}{\xi_1(t)}\left[1 + \frac{1}{\Omega_1(t)}\kappa_x^2 \ln\left(\kappa_x^2\right)\right], \qquad (20)$$

with

$$\Omega_d(t) = \left|W_{-1}\left(-4dC_\psi^2 \frac{\langle\tau\rangle}{t}\right)\right|,$$

$$\xi_d(t) = \sqrt{\tau_0^2\langle v^2\rangle \frac{t\Omega_d(t)}{d\langle\tau\rangle}}, \qquad (21)$$

where here and for the following Lorentz gas $\langle v^2\rangle = V^2$. The walker's position PDF in d spatial dimensions is given by the inverse Fourier transform

$$P_d(\mathbf{r}, t) = \int \frac{d^d\kappa}{(2\pi)^d}\tilde{P}_d(\mathbf{\kappa}, t)\cos\left[\frac{2(\mathbf{\kappa}\cdot\mathbf{r})}{\xi_d(t)}\right]. \qquad (22)$$

Inserting Eq. (20) into Eq. (22) results in

$$P_1(x, t) = \frac{1}{\sqrt{\pi\xi_1^2(t)}}\exp\left(-\frac{x^2}{\xi_1^2(t)}\right)$$
$$\times\left\{1 + \frac{1}{\Omega_1(t)}\left[[2 - \gamma - \ln(4)]\left(\frac{1}{2} - \frac{x^2}{\xi_1^2(t)}\right)\right.\right.$$
$$\left.\left. - \frac{1}{2}M^{(1,0,0)}\left(-1; \frac{1}{2}; \frac{x^2}{\xi_1^2(t)}\right)\right]\right\}. \qquad (23)$$

The subscript 1 stands for one dimension, namely, this result should hold for the stadium channel when we coarse grain over the channel's width. We see some similarities to the problem of summation of IID RVs. For example, Kummer's function appears in both problems as a correction to the leading term. There is however a major difference between the two cases: Here $P_d(\mathbf{r}, t) = 0$ for $|\mathbf{r}| > Vt$, which is different from the problem of summation of IID RVs. This is clearly due to the particles' finite speed. For the two-dimensional Lorentz gas model with two or four infinite horizons we have

$$F_2(\mathbf{v}) = \frac{1-q}{4}\{[\delta(v_x - V) + \delta(v_x + V)]\delta(v_y)$$
$$+ \delta(v_x)[\delta(v_y - V) + \delta(v_y + V)]\}$$
$$+ \frac{q}{4}\left\{\left[\delta\left(v_x - \frac{V}{\sqrt{2}}\right) + \delta\left(v_x + \frac{V}{\sqrt{2}}\right)\right]\right.$$
$$\left.\times\left[\delta\left(v_y - \frac{V}{\sqrt{2}}\right) + \delta\left(v_y + \frac{V}{\sqrt{2}}\right)\right]\right\}, \qquad (24)$$

where $q \geqslant 0$ is a parameter to be determined later, which encodes the probability of a particle to be found in the far tail of the diagonal corridors (for two open horizons, a cross shape, one has $q = 0$). We get, from Eq. (14),

$$\tilde{P}_2(\mathbf{\kappa}, t) \simeq \frac{4e^{-\kappa_x^2 - \kappa_y^2}}{\xi_2^2(t)}\left\{1 + \frac{1-q}{\Omega_2(t)}\left[\kappa_x^2 \ln\left(\kappa_x^2\right) + \kappa_y^2 \ln\left(\kappa_y^2\right)\right]\right.$$
$$+ \frac{q}{2\Omega_2(t)}(\kappa_x + \kappa_y)^2 \ln\left[\frac{1}{2}(\kappa_x + \kappa_y)^2\right]$$
$$\left.+ \frac{q}{2\Omega_2(t)}(\kappa_x - \kappa_y)^2 \ln\left[\frac{1}{2}(\kappa_x - \kappa_y)^2\right]\right\}. \qquad (25)$$

We use a $\pi/4$ rotation transformation $\kappa_\pm = (\kappa_x \pm \kappa_y)/\sqrt{2}$ to calculate the integrals over the last two terms in Eq. (25) and obtain

$$P_2(\mathbf{r}, t) \simeq \frac{1}{\pi\xi_2^2(t)}\exp\left(-\frac{x^2 + y^2}{\xi_2^2(t)}\right)$$
$$\times\left\{1 + \frac{1}{\Omega_2(t)}\left[[2 - \gamma - \ln(4)]\left(1 - \frac{x^2 + y^2}{\xi_2^2(t)}\right)\right.\right.$$
$$- \frac{1-q}{2}M^{(1,0,0)}\left(-1; \frac{1}{2}; \frac{x^2}{\xi_2^2(t)}\right)$$
$$- \frac{1-q}{2}M^{(1,0,0)}\left(-1; \frac{1}{2}; \frac{y^2}{\xi_2^2(t)}\right)$$

$$-\frac{q}{2}M^{(1,0,0)}\left(-1;\frac{1}{2};\frac{(x+y)^2}{2\xi_2^2(t)}\right)$$

$$-\frac{q}{2}M^{(1,0,0)}\left(-1;\frac{1}{2};\frac{(x-y)^2}{2\xi_2^2(t)}\right)\bigg]\bigg\}, \quad (26)$$

where the subscript 2 stands for two dimensions. This solution is presented in Figs. 2 and 3, with the relevant parameters, namely, τ_0, $\langle\tau\rangle$, C_ψ, and q, obtained from $\psi(\tau)$ [more precisely, we extract them from CDF(τ)]. Thus, we continue with deriving exact expressions for the distribution of traveling times $\psi(\tau)$ for the Lorentz gas model with two or four open infinite corridors and for the stadium channel model. To refrain from cumbersome formulas, we omit some of the next section's derivations. Refer to Appendix D for more details.

IV. DISTRIBUTION OF TRAVELING TIMES

A. Lorentz gas model

To obtain the distribution of traveling times we define a two-dimensional cubic lattice of constant 1 occupied with circular scatterers of radius R such that the center of each circle is located at a grid point [see Figs. 1(a) and 1(b)]. Let the lattice coordinates of each scatterer be (n, m), where n and m are integers. We focus on the origin and assume that the particle has just collided with the $(0,0)$ scatterer. We define the collision's impact parameter and recoil direction as b and β, respectively [see Fig. 6(a)], where the ranges of values for these two parameters are $[-R, R]$ and $[0, 2\pi)$, respectively. We denote by $\tau_{n,m}^*(b, \beta, R)$ the time duration until the following collision, and since $V = 1$ it is also the distance traveled. Here we assume that the next scatterer to be collided with is the (n, m) one. The expression obtained for $\tau_{n,m}^*(b, \beta, R)$ is

$$\tau_{n,m}^*(b, \beta, R) = n\cos(\beta) + m\sin(\beta) - \sqrt{R^2 - b^2}$$
$$- \sqrt{R^2 - [m\cos(\beta) - n\sin(\beta) - b]^2}. \quad (27)$$

We then write the PDF $\psi(\tau)$ as

$$\psi(\tau) = \sum_{n,m}\int_{\beta_{n,m}^{\min}(R)}^{\beta_{n,m}^{\max}(R)}\frac{d\beta}{2\pi}\int_{b_{n,m}^{\min}(\beta,R)}^{b_{n,m}^{\max}(\beta,R)}\frac{db}{2R}\delta[\tau - \tau_{n,m}^*(b, \beta, R)], \quad (28)$$

where the factors of $1/2\pi \times 1/2R$ are the distributions of β and b, respectively, which are both uniform due to ergodicity [2]. In Eq. (28) the summation is carried over all relevant integers (see Fig. 7) and the integration boundaries (IBs) need to be found. Therefore, we define the discriminant of Eq. (27),

$$\Delta_{n,m}(b, \beta, R) = R^2 - [m\cos(\beta) - n\sin(\beta) - b]^2. \quad (29)$$

Our starting point for obtaining the IBs is to notice that the rooted quantities in Eq. (27) must be positive. Actually, $R^2 - b^2 \geqslant 0$ means that the particle path indeed intersects the $(0,0)$ circle, which is an initial assumption here, and a positive discriminant in Eq. (29) means that the particle does collide with the (n, m) scatterer. However, in order for the particle to reach the (n, m) scatterer, it must as well not collide with another circle along its path. We therefore use a system of inequalities which are drawn from Eq. (29) to determine β and
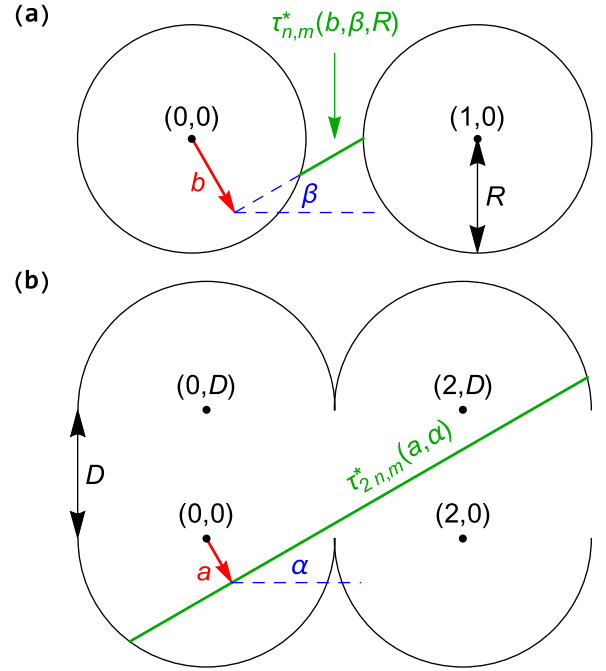

FIG. 6. The parameters which determine the trajectory's length for (a) the Lorentz gas model and (b) the stadium channel model. For the Lorentz gas, the lattice coordinates of the next scatterer to be collided with are denoted by (n, m), the recoil angle after the previous collision is β, and the impact parameter is b. In this sketch, we used $n = 1$, $m = 0$, $\beta = \pi/6$, $b = -0.3$, and $R = 0.4$, which correspond to $\tau_{n,m}^*(b, \beta, R) \approx 0.255$ (the lattice constant is 1). For the stadium channel, we denote by $(2n, m)$ the lattice site of the next stadium to be collided with, where α is the recoil angle after the previous collision, and a is an impact parameter. Here we used $n = 1$, $m = D$, $\alpha = \pi/6$, $a = -0.4$, and $D = 1$, which correspond to $\tau_{2n,m}^*(a, \alpha) \approx 4.11$ (the semicircles' radius is 1).

b's IBs. Assuming that $1/\sqrt{8} \leqslant R < 1/2$, one has a single pair of infinite corridors and the particle can only reach scatterers with lattice indices that obey $n = 1$ or $m = 1$ [see the textured colored circles in Fig. 7(a)]. Symmetry considerations allow us to break the problem into eight areas composed of three components each, and we choose to focus on $m = 1$ and $n \geqslant 0$ [see the black rectangle-encircled area in Fig. 7(a)]. This area's first component is the nearest-neighbor scatterer $(0,1)$. Here Eq. (29) suggests that b obeys

$$\Delta_{0,1}(b, \beta, R) \geqslant 0. \quad (30)$$

The above condition ensures that the particle does collide with the scatterer $(0,1)$ on the next collision. In addition, one should intersect this domain with $|b| \leqslant R$ to ensure that the particle indeed originated from the $(0,0)$ scatterer. Similarly, for the second component, the next-nearest-neighbor scatterer $(1,1)$, the system of inequalities which stems from Eq. (29) reads

$$\Delta_{1,1}(b, \beta, R) \geqslant 0,$$
$$\Delta_{1,0}(b, \beta, R) \leqslant 0, \quad (31)$$
$$\Delta_{0,1}(b, \beta, R) \leqslant 0,$$

and of course $|b| \leqslant R$ as before. This ensures that the particle collides with the $(1,1)$ scatterer (first condition), but not with
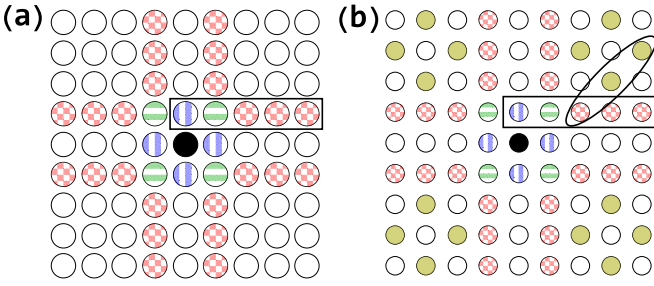
FIG. 7. In the Lorentz gas, a tracer particle right after a collision with the origin circle (solid black) can hit only the colored scatterers. These are made of three distinct groups: four nearest neighbors (vertical blue stripes), four next to nearest neighbors (horizontal green stripes), and eight clusters of distant neighbors (crosshatch red). The white circles are inaccessible for the particle. (a) Given a lattice constant 1, for a scatterers' radius of $R = 0.4$, one has two directions for possible infinite trajectories, directed with the lattice axes. (b) For a scatterers' radius of $R = 0.3$, two diagonal infinite directions are added, and the particle can now reach the yellow (light gray) scatterers. When calculating the cumulative distribution function of the traveling times between collisions, we sum the contribution of each scatterer to the trajectories' space (see Sec. IV). Exploiting the noticeable symmetry, we focus on (a) the black rectangle-encircled area and additionally (b) the black ellipse-encircled area when R is decreased.

the (1,0) or the (0,1) circles (second and third conditions, respectively) that will otherwise block its path. Finally, the third component in this area is the distant-neighbor cluster $n > 1$, which is dominated by the inequalities

$$
\begin{aligned}
\Delta_{n,1}(b, \beta, R) &\geqslant 0, \\
\Delta_{1,0}(b, \beta, R) &\leqslant 0, \\
\Delta_{n-1,1}(b, \beta, R) &\leqslant 0,
\end{aligned}
\tag{32}
$$

as well as $|b| \leqslant R$. This ensures that the particle collides with the $(n, 1)$ scatterer, but avoids the $(1,0)$ or the $(n - 1, 1)$ ones, which can block its path. Analyzing these inequalities in Appendix D, we obtain

$$
\beta_{n,1}^{\min}(R) = \sin^{-1}\left(\frac{1}{\sqrt{n^2 + 1}}\right) - \sin^{-1}\left(\frac{2R}{\sqrt{n^2 + 1}}\right)
\tag{33}
$$

for the lower β IB,

$$
\beta_{n,1}^{\max}(R) = \begin{cases} \pi/2, & n = 0 \\ \pi/4, & n = 1 \\ \beta_{n-2,1}^{\min}(R), & n > 1 \end{cases}
\tag{34}
$$

for the upper β IB, and

$$
b_{n,1}^{\min}(\beta, R) = \begin{cases} \cos(\beta) - n\sin(\beta) - R, & \beta_{n,1}^{\min}(R) \leqslant \beta \leqslant \beta_{n,1}^{\text{sep}}(R) \\ R - \sin(\beta), & \beta_{n,1}^{\text{sep}}(R) \leqslant \beta \leqslant \beta_{n,1}^{\max}(R), \end{cases}
$$

$$
b_{n,1}^{\max}(\beta, R) = \begin{cases} R, & \beta_{n,1}^{\min}(R) \leqslant \beta \leqslant \beta_{n,1}^{\text{sep}}(R) \\ \cos(\beta) - (n-1)\sin(\beta) - R, & \beta_{n,1}^{\text{sep}}(R) \leqslant \beta \leqslant \beta_{n,1}^{\max}(R) \end{cases}
\tag{35}
$$

for the IBs of b, where

$$
\beta_{n,1}^{\text{sep}}(R) = \begin{cases} \pi/2, & n = 0 \\ \beta_{n-1,1}^{\min}(R), & n > 0. \end{cases}
\tag{36}
$$

Equations (33)–(36) together with Eq. (28) provide a full description of $\psi(\tau)$ and alternatively, by an integration over τ, a full description of CDF(τ). Figure 8(a) depicts the CDF obtained from these equations for $R = 0.4$ with its respective numerical simulation counterpart, where an excellent match can be seen. With these equations in mind, we derive an exact expression for τ_0, and numerical values of $\langle \tau \rangle$ and C_ψ for $R = 0.4$ (see Appendix E). For τ_0 we obtain

$$
\tau_0^2 = \frac{2}{\pi R}(1 - 2R)^2.
\tag{37}
$$

This matches the limiting result obtained in Ref. [2] for $R \to 1/2$. It is also in perfect agreement with our previous exact result for τ_0, which we obtained in Ref. [23] using a different indirect approach. For the aforementioned numerical values, we get $\langle \tau \rangle \approx 0.621\,55$ and $C_\psi \approx 4.4802 \times 10^{-4}$, where the former has a relative error of 0.021% compared to the known rigorous result

$$
\langle \tau \rangle = \frac{1 - \pi R^2}{2R},
\tag{38}
$$

which is mentioned in [20]. These values provide excellent results for the numerical simulations of the position's PDF when used as an input for the Lévy walk approximation, as seen in Figs. 2 and 9.

Next we compute the case of four open horizons for the Lorentz gas model (see Figs. 3 and 10). Assuming that $\sqrt{20} \leqslant R < 1/\sqrt{8}$, there are two additional open horizons, namely, the two main diagonals. It turns out that the formulas we obtained above for the $m = 1$ and $n \geqslant 0$ stripe are valid here as well, excluding the (2,1) scatterer. Since R is now smaller, possible trajectories emerge for the diagonal directions, and we choose to focus on movements which end at the $(m + 1, m)$ circles where $m \geqslant 1$ [see the ellipse-encircled area in Fig. 7(b)]. Thus, we need to adjust the (2,1) scatterer's upper IB, as it is now counted in two distinct sets of scatterers. The specifics are detailed in Appendix D, and we obtain the correction

$$
\beta_{2,1}^{\max}(R) = \sin^{-1}(2R).
\tag{39}
$$

The diagonal area's inequalities are obtained yet again from Eq. (29). For the diagonal part of (2,1) we have

$$
\Delta_{2,1}(b, \beta, R) \geqslant 0.
\tag{40}
$$

(a) CDF(τ)

— Lorentz gas   -- Theory   ---- Large τ limit
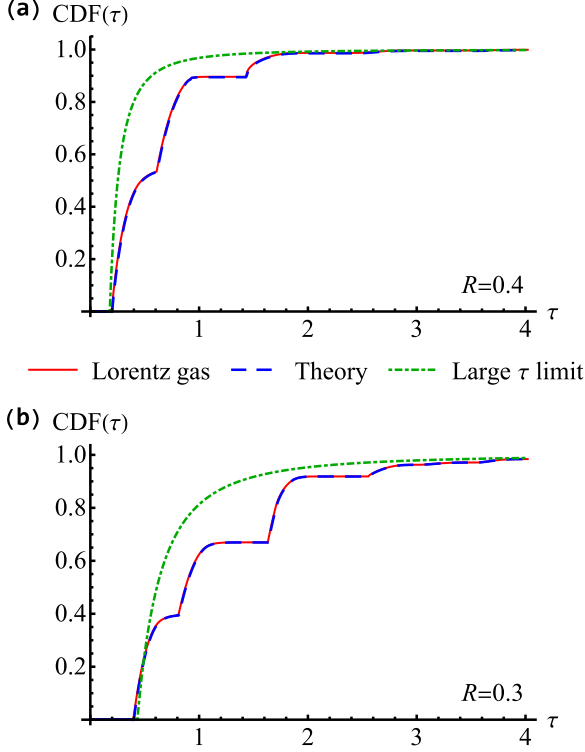
(b) CDF(τ)

FIG. 8. The cumulative distribution function of intercollision times for the Lorentz gas model derived in Sec. IV, its respective result obtained from the numerical simulations, and the large-τ limit given by CDF(τ) $\simeq 1 - \tau_0^2/2\tau^2$. The scatterers radius is (a) $R = 0.4$ and (b) $R = 0.3$, corresponding to two and four open infinite corridors, respectively (the lattice constant is 1). The numerical histograms are made of a single long trajectory containing 10^6 collisions.

$$
b_{m+1,m}^{\min}(\beta, R) = \begin{cases} (m-1)\cos(\beta) - m\sin(\beta) + R, & \beta_{m+1,m}^{\min}(R) \leqslant \beta \leqslant \beta_{m+1,m}^{\text{sep}}(R) \\ -R, & \beta_{m+1,m}^{\text{sep}}(R) \leqslant \beta \leqslant \beta_{m+1,m}^{\max}(R), \end{cases}
$$

$$
b_{m+1,m}^{\max}(\beta, R) = \begin{cases} \cos(\beta) - \sin(\beta) - R, & \beta_{m+1,m}^{\min}(R) \leqslant \beta \leqslant \beta_{m+1,m}^{\text{sep}}(R) \\ m\cos(\beta) - (m+1)\sin(\beta) + R, & \beta_{m+1,m}^{\text{sep}}(R) \leqslant \beta \leqslant \beta_{m+1,m}^{\max}(R) \end{cases}
\tag{44}
$$

for the IBs of b, where

$$
\beta_{m+1,m}^{\text{sep}}(R) = \begin{cases} \sin^{-1}(2R), & m = 1 \\ \beta_{m,m-1}^{\max}(R), & m > 1. \end{cases}
\tag{45}
$$

Using Eqs. (42)–(45), we calculate the CDF(τ) for $R = 0.3$, which is plotted in Fig. 8(b), where an excellent match to the simulations can be seen. We derive from these equations an exact expression for τ_0, obtaining

$$
\tau_0^2 = \frac{2}{\pi R}(1 - 2R)^2 + \frac{\sqrt{2}}{\pi R}(1 - \sqrt{8}R)^2.
\tag{46}
$$

Equation (46) is used to define q, which determines the relevant weight of the velocities' PDF in the Lévy walk formalism, along respective directions of the infinite corridors. Recalling that q determines the probability of a particle to be at the diagonal corridors, we *define* this parameter as the ratio between the diagonal corridors' contribution for the behavior

This circle is similar to the (0,1) one in the previous case, as there are no possible obstacles for the (diagonal) nearest neighbor. The rest of the IBs are found by analyzing

$$
\Delta_{m+1,m}(b, \beta, R) \geqslant 0,
$$
$$
\Delta_{m,m-1}(b, \beta, R) \leqslant 0,
$$
$$
\Delta_{1,1}(b, \beta, R) \leqslant 0
\tag{41}
$$

in a similar way as was done previously, where $m > 1$. This time, the possible scatterers to block the particle's path are $(m, m-1)$ and $(1,1)$. We obtain

$$
\beta_{m+1,m}^{\max}(R) = \sin^{-1}\left(\frac{m}{\sqrt{m^2 + (m+1)^2}}\right)
$$
$$
+ \sin^{-1}\left(\frac{2R}{\sqrt{m^2 + (m+1)^2}}\right)
\tag{42}
$$

for the upper β IB,

$$
\beta_{m+1,m}^{\min}(R) = \begin{cases} \sin^{-1}(2R), & m = 1 \\ \sin^{-1}(2R), & m = 2 \\ \beta_{m-1,m-2}^{\max}(R), & m > 2 \end{cases}
\tag{43}
$$

for the lower β IB, and

$\psi(\tau) \sim \tau^{-3}$ and the overall τ_0^2 and find that

$$
q = \frac{(1 - \sqrt{8}R)^2}{\sqrt{2}(1 - 2R)^2 + (1 - \sqrt{8}R)^2}
\tag{47}
$$

when $1/\sqrt{20} \leqslant R < 1/\sqrt{8}$. We also get from $\psi(\tau)$ numerical values for $\langle \tau \rangle$ and C_ψ for this specific value of R (see Appendix E). We find that $\langle \tau \rangle \approx 1.1947$, with a relative error of 0.059% from the rigorous result (38), and also $C_\psi \approx 1.5250 \times 10^{-2}$. These values provide excellent results for the numerical simulations of the position's PDF when used as an input for the Lévy walk approximation, as seen in Figs. 3 and 10.

B. Stadium channel model

Let us now precisely define the notation used for the stadium channel. As we have lower and upper boundaries for
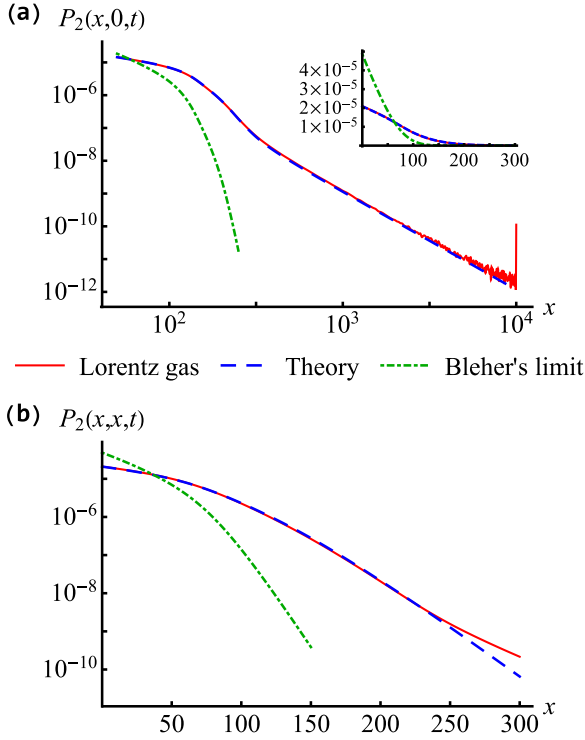
FIG. 9. Cross sections of the probability density function of the Lorentz gas with $R = 0.4$ (Fig. 2) for (a) $y = 0$ and (b) $y = x$. The green dot-dashed curve is Bleher's Gaussian limit, solid red is the Lorentz gas numerical simulations, and dashed blue is Eq. (26) with $q = 0$. Deviations in the $x \approx 300$ area of the $y = x$ case are caused by the finite number of sampled trajectories approximately equal to 10^9.
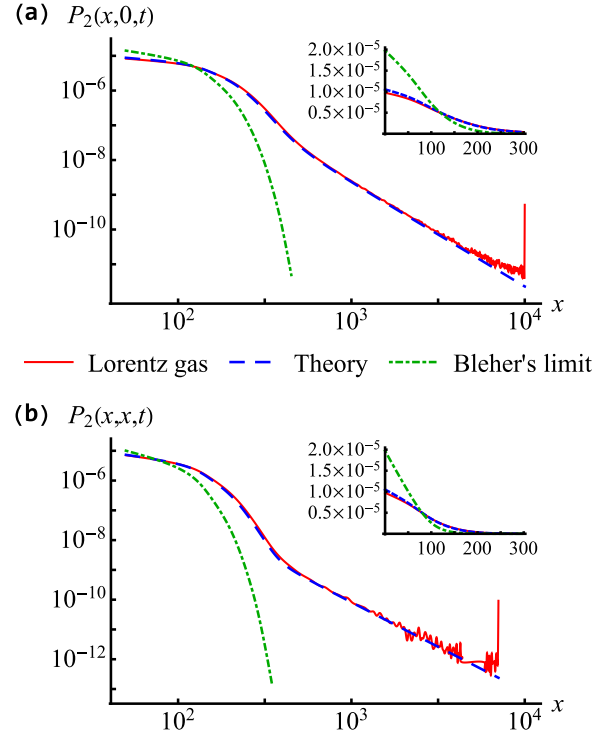

FIG. 10. Cross sections of the probability density function of the Lorentz gas with $R = 0.3$ (Fig. 3) for (a) $y = 0$ and (b) $y = x$. The green dot-dashed curve is Bleher's Gaussian limit, solid red is the Lorentz gas numerical simulations, and dashed blue is Eq. (26) with $q > 0$, which is given by Eq. (47). The curves match perfectly.

this pipe structure, we define two parallel one-dimensional straight lattices of constant 2 which are separated by a distance D. These are occupied by circular stadiums of radius 1 such that the center of each stadium is located at a grid point [see Fig. 1(c)]. Let $(2n, m)$ denote the center of a given stadium, where n is an integer and m can take two possible values, 0 and D [see Fig. 6(b)]. We focus on the origin and assume that the particle has just been scattered from the lower wall's $n = 0$ stadium. We define the collision's impact parameter and recoil direction as a and α, respectively [see Fig. 6(b)], where the ranges of values for these two parameters are $[-1, 1]$ and $[0, 2\pi)$, respectively. We denote by $\tau_{2n,m}^*(a, \alpha)$ the time duration until the following collision, and since $V = 1$ it is also the distance traveled. Here the next stadium to be collided with is $(2n, m)$, where the integer n can be regarded as a semicircle's numbering, while m denotes the top or bottom wall. Notice that the particle is able to reach the stadium of origin, namely, $n = m = 0$. We obtained, for $\tau_{2n,m}^*(a, \alpha)$,

$$\tau_{2n,m}^*(a, \alpha) = 2n\cos(\alpha) + m\sin(\alpha) + \sqrt{1 - a^2}$$
$$+ \sqrt{1 - [m\cos(\alpha) - 2n\sin(\alpha) - a]^2}. \quad (48)$$

The particle can only reach semicircles located in the upper row, or the origin stadium. Symmetry considerations allow us to break the problem into two areas, and we choose to

focus on $n \geqslant 0$ [see Fig. 1(c)]. We then write the PDF $\psi(\tau)$ as

$$\psi(\tau) = 4 \int_{\alpha_{0,0}^{\min}}^{\alpha_{0,0}^{\max}} \frac{d\alpha}{2\pi} \int_{a_{0,0}^{\min}(\alpha)}^{a_{0,0}^{\max}(\alpha)} \frac{da}{2} \delta[\tau - \tau_{0,0}^*(a, \alpha)]$$
$$+ 4 \sum_{n=0}^{\infty} \int_{\alpha_{2n,D}^{\min}}^{\alpha_{2n,D}^{\max}} \frac{d\alpha}{2\pi} \int_{a_{2n,D}^{\min}(\alpha)}^{a_{2n,D}^{\max}(\alpha)} \frac{da}{2} \delta[\tau - \tau_{2n,D}^*(a, \alpha)],$$

$$(49)$$

where the factors of $1/2\pi \times 1/2$ are the distributions of α and a, respectively. As the corresponding parameters of the Lorentz gas β and b are known to be uniform [2], here we *assume* the same for α and a. The particle can travel into the $n \leqslant 0$ area, as well as from top to bottom, hence the multiplicative factor of 4. To obtain the IBs, we use a similar scheme as for the Lorentz gas. However, there is a major difference between the two cases. Due to convexity, there are two possible points of origin or collision for the particle's trajectory. In the Lorentz gas case, there was no need to differentiate between these two options during the calculations; thus we used the discriminant to tell whether a given scatterer was hit or missed. In the stadium channel case, the discriminant is of no use as the stadiums are semicircles, and the discriminant cannot differentiate between a true stadium and a continuation of its wall to a complete circle. Therefore, here we define the vertical axis coordinate of the origin and target points $y_0(a, \alpha)$

and $w_{2n,m}(a, \alpha)$, respectively,

$$y_0(a, \alpha) = \sqrt{1 - a^2} \sin(\alpha) + a \cos(\alpha),$$
$$w_{2n,m}(a, \alpha) = y_0(a, \alpha) + \tau_{2n,m}^*(a, \alpha) \sin(\alpha), \quad (50)$$

and extract the needed inequalities from them instead. This time we demand that $w_{2n,m}(a, \alpha) - m$ be non-negative for the upper stadiums and nonpositive for the origin stadium. This replaces the demand of a positive discriminant in the Lorentz gas case. We also demand that $y_0(a, \alpha)$ be nonpositive, which is analogous to $|b| \leqslant R$ in the Lorentz gas case. The first component of the chosen area is the origin semicircle, for which Eq. (50) dictates that a obey

$$y_0(a, \alpha) \leqslant 0, \quad w_{0,0}(a, \alpha) \leqslant 0. \quad (51)$$

The upper IB of α is set to $\pi/2$ and the lower to $-\pi/2$, which is possible due to symmetry. The second component is the $n = 0$ upper stadium, for which we have

$$y_0(a, \alpha) \leqslant 0, \quad w_{0,D}(a, \alpha) \geqslant D. \quad (52)$$

The upper IB of α is set again to $\pi/2$ from symmetry considerations and the lower is found by analyzing Eq. (52). Finally, in order for the particle to reach the $n > 0$ upper semicircles, it must not collide with another stadium wall along its path.

$$a_{2n,D}^{min}(\alpha) = \begin{cases} D\cos(\alpha) - (2n+1)\sin(\alpha), & \alpha_{2n,D}^{min} \leqslant \alpha \leqslant \alpha_{2n,D}^{sep} \\ -\sin(\alpha), & \alpha_{2n,D}^{sep} \leqslant \alpha \leqslant \alpha_{2n,D}^{max}, \end{cases}$$
$$a_{2n,D}^{max}(\alpha) = \begin{cases} \sin(\alpha), & \alpha_{2n,D}^{min} \leqslant \alpha \leqslant \alpha_{2n,D}^{sep} \\ D\cos(\alpha) - (2n-1)\sin(\alpha), & \alpha_{2n,D}^{sep} \leqslant \alpha \leqslant \alpha_{2n,D}^{max} \end{cases} \quad (57)$$

for the IBs of a, where

$$\alpha_{2n,D}^{sep} = \begin{cases} \pi/2, & n = 0 \\ \alpha_{2n-2,D}^{min}, & n > 0. \end{cases} \quad (58)$$

Figure 11 depicts the CDF obtained from Eqs. (55)–(58) for $D = 1$ with its respective numerical simulations counterpart, where an excellent match can be seen. We also use these to derive an exact expression for τ_0, and the numerical values of $\langle \tau \rangle$ and C_ψ for $D = 1$ (see Appendix E). For τ_0 we obtain

$$\tau_0 = \sqrt{\frac{2}{\pi}}D. \quad (59)$$

We also find $\langle \tau \rangle \approx 2.570\,16$, with a relative error of 0.005% from the simulation result $\langle \tau \rangle \approx 2.570\,31$, and $C_\psi \approx 1.0903 \times 10^{-5}$. However, these values do not provide a correct description for the Lévy walk approximation, due to the renewal assumption being nullified by strong temporal correlations discussed below. Nonetheless, one can fit the Lévy walk approximation to the simulations data using a two-parameter fit ($C_\psi^2 \langle \tau \rangle$ and $\langle \tau \rangle / \tau_0^2$), and thus find effective constants. These turn out to describe the problem well, as seen in Fig. 4(a). We have verified that the values obtained for the constants by fitting do not change over time [see Fig. 4(b)].

We would like to direct the reader's attention to the different geometry of the Lorentz gas CDF and the stadium channel

For this third component, the conditions are

$$y_0(a, \alpha) \leqslant 0, \quad w_{2n,D}(a, \alpha) \geqslant D,$$
$$w_{2n-2,D}(a, \alpha) \leqslant D, \quad w_{0,0}(a, \alpha) \geqslant 0. \quad (53)$$

The first line in Eq. (53) ensures that the particle originated from and arrived at the correct points, while the second line prevents the top $2n - 2$ and bottom $n = 0$ semicircles from blocking the particle's path. Analyzing these inequalities in Appendix D, we obtain for the origin (namely $n = m = 0$) stadium as the target,

$$-1 \leqslant a \leqslant -\sin(\alpha), \quad 0 \leqslant \alpha \leqslant \frac{\pi}{2}$$
$$-1 \leqslant a \leqslant \sin(\alpha), \quad -\frac{\pi}{2} \leqslant \alpha \leqslant 0, \quad (54)$$

and for the top $n \geqslant 0$ and $m = D$ row of stadiums as targets,

$$\alpha_{2n,D}^{min} = \tan^{-1}\left(\frac{D}{2n+2}\right) \quad (55)$$

for the lower α IB,

$$\alpha_{2n,D}^{max} = \begin{cases} \pi/2, & n = 0, 1 \\ \alpha_{2n-4,D}^{min}, & n > 1 \end{cases} \quad (56)$$

for the upper α IB, and

CDF. Both CDFs have qualitatively different shapes, being convex (concave) for the Lorentz gas (stadium channel) [see Fig. 8 (Fig. 11)]. This might be related to the scatterers' shape in the two models, which is convex (concave) for the Lorentz gas (stadium channel). We believe that this phenomenon is
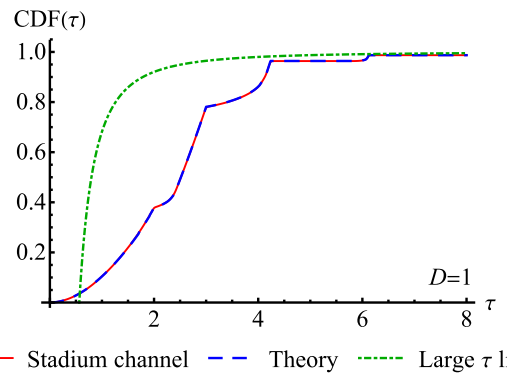

FIG. 11. The cumulative distribution function of intercollision times for the stadium channel model derived in Sec. IV, its respective result obtained from the numerical simulations, and the large-τ limit given by $\mathrm{CDF}(\tau) \simeq 1 - \tau_0^2/2\tau^2$. The walls of semicircles are separated a distance $D = 1$ from each other and the radius of a stadium is 1. The numerical histograms are made of a single long trajectory containing 10^6 collisions.
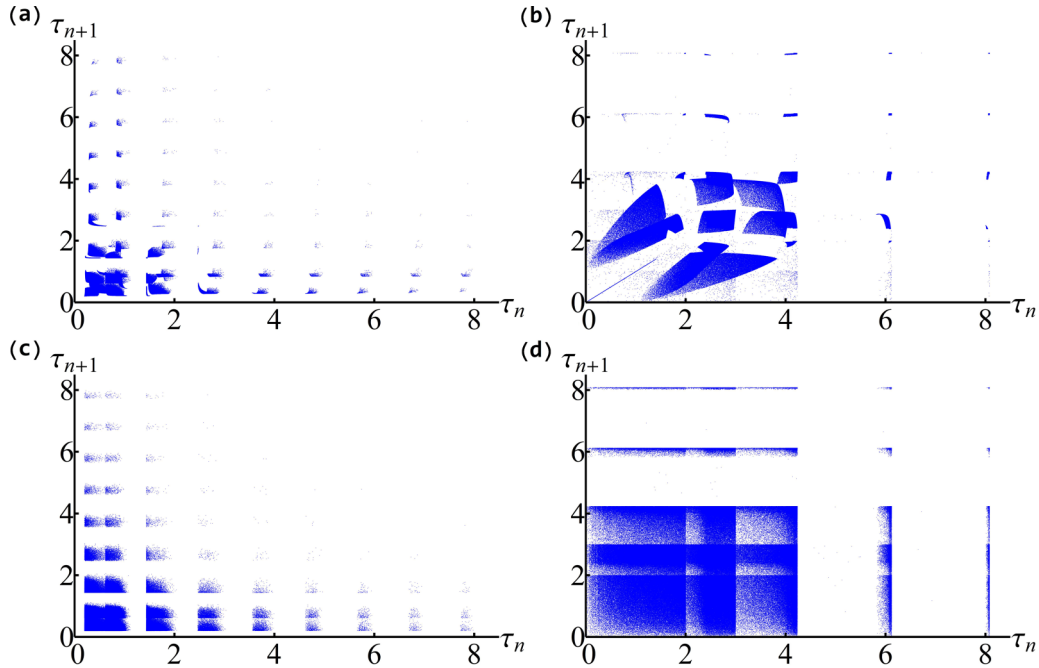
FIG. 12. Correlations of the traveling times between collisions. Shown are points of the form (τ_n, τ_{n+1}), where τ_n is the nth flight duration. Depicted are numerical realizations of (a) the Lorentz gas model with two open horizons ($R = 0.4$) and (b) the stadium channel model ($D = 1$). Also presented are points drawn from the intercollision times' CDF obtained analytically for (c) the Lorentz gas with two infinite corridors (28) ($R = 0.4$) and (d) the stadium channel (49) ($D = 1$). Each plot consists of approximately 10^6 points. The Lorentz gas displays strong similarity between repeated draws and the simulation data, meaning that the renewal condition is indeed fulfilled. However, for the stadium channel the patterns are substantially different, which means that here the condition fails. See additional discussion in Sec. V.

general as the geometry of the scattering centers is clearly embedded in this basic distribution; however, we leave this intriguing point for future work.

V. DISCUSSION AND SUMMARY

Returning to Sec. II, we address an issue we previously disregarded with the Lambert scaling approach. The reader may have noticed that the choice of the scaling function $\Omega(t)$ is not unique, but can be determined up to a constant. More accurately, one may choose to separate the logarithmic term into two at an arbitrary point, as one can always write

$$\ln\left(\frac{2C_f^2\bar{k}^2}{N\Omega(N)}\right) = \ln\left(\frac{2C_f^2\eta}{N\Omega(N)}\right) + \ln\left(\frac{\bar{k}^2}{\eta}\right). \quad (60)$$

Recall that we used the first term on the right-hand side of Eq. (60) with $\eta = 1$ to derive the Lambert scaling [see Eq. (7)] while expanding the $\bar{k}^2$-containing exponential term [see Eq. (10)]. Here η is a free parameter which cannot be determined uniquely by the aforementioned steps alone. We found that taking $\eta = 1$ produces good results for $P(x, N)$ and alternatively for $P_d(\mathbf{r}, t)$ (see Figs. 4, 5, 9, and 10). Of course, if one sums the complete asymptotic series [which is given to subleading order by Eq. (11)] η vanishes, but then the result diverges.

Looking back at Figs. 2 and 3, the reader may notice that the shape at $|\mathbf{r}| = r \sim t$ of the analytical results mismatches that of the simulations. This can be explained via our scaling assumption $u \sim k^2 \ln(k)$, which suggests that $k \gg u$, namely,

our approximation is for displacement that obeys $r \ll t$. Nonetheless, it holds well at the distribution's infinite corridors: $y = 0$ and $x = 0$ for two open horizons and additionally $y = x$ and $y = -x$ for four. Utilizing the infinite covariant density [32], which has recently been gaining attention, could probably supply one with tools to approximate edge phenomena such as this.

Finally, we direct the reader to interesting correlation patterns of the stadium channel model, seen in Fig. 12(b). We plot points of consecutive traveling times (τ_{n+1}, τ_n), for the Lorentz gas and the stadium channel, obtained from numerical samplings and analytical results. Both models exhibit a phenomenon of clear pointless areas on the graph, which is caused by the plateaus in the CDFs (Figs. 8 and 11), which in turn correspond to a vanishing PDF $\psi(\tau)$. Indeed, due to the discrete nature of the scattering centers, there exist certain durations of travel that are not possible (in a disordered system this nonanalytical behavior would vanish). Technically speaking, long traveling times become semidiscrete, which is due to small parameter spaces $\{b, \beta\}$ [see Eqs. (33)–(35)] and $\{a, \alpha\}$ [see Eqs. (55)–(57)] which support these long trajectories. Interesting patterns emerge from roughly $\tau_n \lesssim 4.25$ for the stadium channel simulations [see Fig. 12(b)]. These patterns suggest a highly correlative system. Indeed, when no correlations are present, one expects to find square-shaped patterns that correspond to the independence of the axes, e.g., as seen for the Lorenz gas case (both analytical and numerical). However, the stadium channel's simulations reveal a complete opposite. Take, for example, the line $\tau_{n+1} = \tau_n$, extending roughly up to $\tau_n \approx 1.5$. Examining the raw
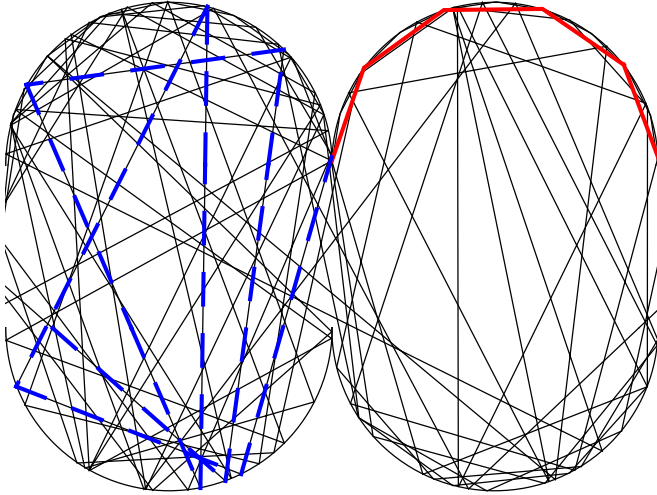
FIG. 13. Piece of trajectory for the stadium channel model, with colored correlative sequences. The right cell shows gallery whispering paths, which are responsible for the $\tau_{n+1} = \tau_n$ line in Fig. 12 (solid thick red). The left cell shows the up and down repetitive movements termed periodic orbits, responsible for the center rectangle-shaped area in Fig. 12 (dashed thick blue) discussed in the text. These types of traps hold the particle in a localized area in the phase space [17], thus invalidating renewals.

data, we found repeated instances of the form $\tau_1, \tau_1, \tau_1, \ldots$, where the number of elements depends on the size of τ_1. Each instance always summed to a value less than or equal to $\pi/2$, the length of a semicircle arc [see Fig. 13 (right cell)]. In these cases, a particle arrives at an almost vertical angle at one end of an arc and then propagates along it, similarly to gallery whispering modes of wave propagation. Other patterns correspond to different repeated instances, e.g., a particle performing periodic orbits [see Fig. 13 (left cell)] will have $\tau_n \approx 2 + D = 3$, which fits the middle rectangle. We computed the correlation functions for both models and found that the Lorentz gas one decays much faster than the stadium channel one (not shown). Indeed, bounds on the temporal decay of the CDFs were obtained, showing that the Lorentz gas one decays with time in a stretched-exponential form [16], while the stadium channel one decays in a polynomial form [17]. Thus, it is not surprising that the renewal condition does not hold for the stadium channel.

In conclusion, we have presented a geometrical method which yields the CDF of traveling times between collision events for billiard systems. We implemented this method for the Lorentz gas with infinite horizon and the stadium channel models. The approach is based on a shadowing effect (as some scatterers cannot be reached), on symmetry, and also on the uniformity of collision parameters (see Figs. 6 and 7). Our analytical and numerical results coincide. The distribution of waiting times has two main features. The first is a power-law decay (1) and the second is its nonanalytical features (see Figs. 8 and 11). The former is due to the infinite horizon and the latter is obviously related to the periodic array of scattering centers. For example, in the infinite horizon Lorentz gas, after a collision event the traveling time of the tracer particle to the next target must be longer than or equal to the distance

between two adjutant scattering centers (in units of unity velocity). This and other dead times implies the observed nonanalytical behavior of the traveling times' distribution. Note that for the channel model arbitrarily short times are possible, due to a gallery whispering path effect [see Fig. 13 (right cell)]. These exhibit a very correlated motion, as a short-time interval between collision events is most likely to be followed by another short interval of the same size [see Fig. 12(b)].

This leads to the second theme of our work: Can one use the distribution of time intervals between collision events to predict the time-dependent probability to find particles at a given position? The answer is system dependent. The technique to make this step is based on the Lévy walk model, in dimension 1 for the stadium channel and 2 for the Lorentz gas. This model makes the assumption of renewal, and we found it works well for the Lorentz gas and not at all for the stadium channel. A tool to check the renewal hypothesis, from an analysis of the paths, is a correlation plot of consecutive waiting times [see Figs. 12(b) and 12(d)], which clearly points out the strong correlations for the stadium channel. However, even the failure of renewal theory does not imply the complete breakdown of the Lévy walk scheme. In this case we introduced effective (or renormalized) parameters for the Lévy walk model obtained by fitting, yielding predictions that are still very useful. In fact, there are general trends in the position's distribution that are universal and nicely predicted by the Lévy walk. These include the fat tail of the spreading packet, sharp cutoffs of the density at $|\mathbf{r}| = Vt$, the Kummer corrections to the Gaussian (which are certainly not small on any reasonable timescale), and the Lambert scaling. The latter is very important since it allowed us to compare finite-time simulations with our theory, while the asymptotic Gaussian form (which exists for the Lorentz gas) is not seen due to superslow convergence problems (see Figs. 9 and 10). One way to understand this behavior is to realize that the billiard systems are operating at a transition point between Lévy and Gauss statistics. Because of the exponent -3 in Eq. (1), the system is essentially behaving as if it is critical in the sense of very sluggish convergence. Roughly speaking and for finite times, the packet of particles' tails exhibits Lévy behavior (a power law with cutoff), while the center part is Gaussian. In the problem of IID RV summation (Sec. II), we encountered a critical slowing down at this borderline case, solved by departing from the $\sqrt{N \ln(N)}$ scaling and replacing it with the Lambert approach.

To map the problem to a Lévy walk, one needs to model the distribution of velocities $F_d(v)$. For the stadium channel this is rather easy, as the model is one dimensional and from symmetry we use a velocity which is either $+V$ or $-V$ with equal probability. For the Lorentz gas, a more careful analysis is needed. As we decrease the size of scatterers, we open more infinite corridors of motion. At first we have four open horizons and this leads to a crosslike shape of the spreading packet (see Fig. 2). Here the velocity distribution in the Lévy walk scheme has a simple structure as the four directions are clearly identical from symmetry. However, when R is made slightly smaller than $1/\sqrt{8}$, we open a new channel but only slightly, meaning that the effective velocity in these directions is statistically reduced compared to the original four corridors

(note that we refer to the distribution of velocities in the Lévy walk and not to the microscopic velocities of the Lorenz gas). The resulting effect is the creation of a British flaglike type of structure for the packet's distribution (see Fig. 3). Thus, we observe a transition from one geometry to another as we vary R. Theoretically, this means that we assign different statistical weights to each group of horizons as in Eq. (26), which is made possible with geometrical considerations leading to the important parameter q in Eq. (47).

APPENDIX A: LEADING BEHAVIOR OF $\tilde{f}(k \to 0)$

We assume that $f(\chi)$ possesses the asymptotic behavior

$$\lim_{\chi \to \pm\infty} f(\chi)|\chi|^{1+\nu} = \chi_0^\nu, \tag{A1}$$

where $\nu > 0$ and $\chi_0 > 0$ are real numbers. The Fourier transform of $f(\chi)$ is defined as

$$\tilde{f}(k) = \int_{-\infty}^{\infty} d\chi \, f(\chi) e^{ik\chi}. \tag{A2}$$

Due to the evenness of $f(\chi)$, $\tilde{f}(k)$ is even and real. Therefore, throughout the following sections we assume that $k \to 0^+$ and use parity to find $\tilde{f}(k \to 0^-)$. As we show below, given a positive integer $\bar{n}$, Eqs. (A1) and (A2) lead to

$$\tilde{f}(k) \simeq \sum_{n=0}^{\bar{n}-1} \frac{(ik)^n}{n!} \langle \chi^n \rangle + \begin{cases} 2\Gamma(-\nu)\cos(\frac{\pi\nu}{2})|\chi_0 k|^\nu, & \bar{n}-1 < \nu < \bar{n} \\ \frac{\pi}{\bar{n}!}(-1)^{(\bar{n}+1)/2}|\chi_0 k|^{\bar{n}}, & \nu = \text{odd } \bar{n} \\ \frac{1}{\bar{n}!}(-1)^{(\bar{n}+2)/2}(\chi_0 k)^{\bar{n}} \ln\left(C_{\bar{n}}^2 \chi_0^2 k^2\right), & \nu = \text{even } \bar{n}, \end{cases} \tag{A3}$$

where $C_{\bar{n}}[f(\chi)]$ is defined in the corresponding section. Using Eqs. (A1) and (A2), we extract all of the converging moments from the Fourier transform integral

$$\tilde{f}(k) = \sum_{n=0}^{\bar{n}-1} \frac{(ik)^n}{n!} \langle \chi^n \rangle + \int_{-\infty}^{\infty} d\chi \, f(\chi) \left[e^{ik\chi} - \sum_{n=0}^{\bar{n}-1} \frac{(ik\chi)^n}{n!} \right] \tag{A4}$$

and consider each of the cases in Eq. (A3) separately.

1. Noninteger ν

Let us assume that $\bar{n} - 1 < \nu < \bar{n}$. In order to find the leading behavior of the second term of Eq. (A4), we consider the limit

$$l_0 = \lim_{k \to 0^+} \frac{1}{k^\nu} \int_{-\infty}^{\infty} d\chi \, f(\chi) \left[e^{ik\chi} - \sum_{n=0}^{\bar{n}-1} \frac{(ik\chi)^n}{n!} \right]. \tag{A5}$$

Using l'Hôpital's rule $\bar{n}$ times yields

$$l_0 = \lim_{k \to 0^+} \frac{\Gamma(-\nu)(-i)^{\bar{n}}}{\Gamma(-\nu+\bar{n})} k^{\bar{n}-\nu} \int_{-\infty}^{\infty} d\chi \, f(\chi) \chi^{\bar{n}} e^{ik\chi}, \tag{A6}$$

where $\Gamma(\cdots)$ is the Gamma function. We use an $\eta = k\chi$ variable change

$$l_0 = \frac{\Gamma(-\nu)(-i)^{\bar{n}}}{\Gamma(-\nu+\bar{n})} \lim_{k \to 0^+} \int_{-\infty}^{\infty} d\eta \, e^{i\eta} \eta^{\bar{n}} \frac{f(\eta/k)}{k^{\nu+1}}. \tag{A7}$$

We now switch the order of the limit and integration while using the asymptotic behavior (A1),

$$l_0 = \frac{\chi_0^\nu \Gamma(-\nu)(-i)^{\bar{n}}}{\Gamma(-\nu+\bar{n})} \int_{-\infty}^{\infty} d\eta \, \frac{e^{i\eta} \eta^{\bar{n}}}{|\eta|^{\nu+1}} = 2\chi_0^\nu \Gamma(-\nu)\cos\left(\frac{\pi\nu}{2}\right), \tag{A8}$$

which proves the first line of Eq. (A3).

2. Integer ν

Let us assume that $\nu = \bar{n}$, where $\bar{n}$ is even. In order to find the leading behavior of the second term of Eq. (A4), we consider the limit

$$l_1 = \lim_{k \to 0^+} \frac{1}{k^{\bar{n}} \ln(k)} \int_{-\infty}^{\infty} d\chi \, f(\chi) \left[e^{ik\chi} - \sum_{n=0}^{\bar{n}-1} \frac{(ik\chi)^n}{n!} \right]. \tag{A9}$$

Using l'Hôpital's rule $\bar{n} + 1$ times produces

$$l_1 = \frac{i^{\bar{n}+1}}{\bar{n}!} \lim_{k \to 0^+} k \int_{-\infty}^{\infty} d\chi \, f(\chi) \chi^{\bar{n}+1} e^{ik\chi}. \tag{A10}$$

Changing the integration variable to $\eta = k\chi$ gives

$$l_1 = \frac{i^{\bar{n}+1}}{\bar{n}!} \lim_{k \to 0^+} \int_{-\infty}^{\infty} d\eta \, e^{i\eta} f\left(\frac{\eta}{k}\right) \left(\frac{\eta}{k}\right)^{\bar{n}+1}. \tag{A11}$$

After switching the order of the limit and integration, the integral exists as a Cauchy principal value and we find

$$l_1 = \chi_0^{\bar{n}} \frac{i^{\bar{n}+1}}{\bar{n}!} \text{P.V.} \int_{-\infty}^{\infty} d\eta \, e^{i\eta} \text{sgn}(\eta) = -\frac{2}{\bar{n}!} (-1)^{\bar{n}/2} \chi_0^{\bar{n}}. \tag{A12}$$

If $\bar{n}$ is odd, we return to Eq. (A8) and take the limit of $\nu \to \bar{n}$, where $\bar{n}$ is odd. We obtain

$$l_1 = \lim_{\nu \to \bar{n}} 2\chi_0^{\nu} \Gamma(-\nu) \cos\left(\frac{\pi \nu}{2}\right) = \frac{\pi}{\bar{n}!} (-1)^{(\bar{n}+1)/2} \chi_0^{\bar{n}}. \tag{A13}$$

To compute the next-order correction for the case of an even $\bar{n}$, we calculate the limit

$$l_2 = \lim_{k \to 0^+} \frac{1}{k^{\bar{n}}} \left\{ \int_{-\infty}^{\infty} d\chi \, f(\chi) \left[e^{ik\chi} - \sum_{n=0}^{\bar{n}-1} \frac{(ik\chi)^n}{n!} \right] + \frac{2}{\bar{n}!} (-1)^{\bar{n}/2} (\chi_0 k)^{\bar{n}} \ln(k) \right\}. \tag{A14}$$

Using l'Hôpital's rule $\bar{n}$ times results in

$$l_2 = \frac{(-1)^{\bar{n}/2}}{\bar{n}!} \lim_{k \to 0^+} \left\{ \int_{-\infty}^{\infty} d\chi \, f(\chi) \chi^{\bar{n}} e^{ik\chi} + 2\chi_0^{\bar{n}} [\ln(k) + H_{\bar{n}}] \right\}, \tag{A15}$$

where $H_{\bar{n}} = \sum_{n=1}^{\bar{n}} \frac{1}{n}$ is the $\bar{n}$th harmonic number. Since $\bar{n}$ is even, the integral in Eq. (A15) can be adjusted to the domain $[0, \infty)$, with $\exp(ik\chi) \to \cos(k\chi)$. We split the adjusted integral at $\chi = \chi_0$:

$$l_2 = \frac{2}{\bar{n}!} (-1)^{\bar{n}/2} \lim_{k \to 0^+} \left\{ \int_0^{\chi_0} d\chi \, f(\chi) \chi^{\bar{n}} \cos(k\chi) + \int_{\chi_0}^{\infty} d\chi \, f(\chi) \chi^{\bar{n}} \cos(k\chi) + \chi_0^{\bar{n}} [\ln(k) + H_{\bar{n}}] \right\}. \tag{A16}$$

We now add and subtract a $\chi_0^{\bar{n}}/\chi^{\bar{n}+1}$ term from $f(\chi)$ in the second integral in Eq. (A16):

$$l_2 = \frac{2}{\bar{n}!} (-1)^{\bar{n}/2} \lim_{k \to 0^+} \left\{ \int_0^{\chi_0} d\chi \, f(\chi) \chi^{\bar{n}} \cos(k\chi) + \int_{\chi_0}^{\infty} d\chi \left[f(\chi) - \frac{\chi_0^{\bar{n}}}{\chi^{\bar{n}+1}} \right] \chi^{\bar{n}} \cos(k\chi) \right.$$
$$\left. + \int_{\chi_0}^{\infty} d\chi \frac{\chi_0^{\bar{n}}}{\chi} \cos(k\chi) + \chi_0^{\bar{n}} [\ln(k) + H_{\bar{n}}] \right\}. \tag{A17}$$

Note that, due to the asymptotics (A1), the second integral above is finite when $k \to 0^+$. The bottom integral in Eq. (A17) can be computed explicitly, after which the limit can be evaluated. Finally, we find

$$l_2 = \frac{2}{\bar{n}!} (-1)^{\bar{n}/2} \left\{ \int_0^{\chi_0} d\chi \, f(\chi) \chi^{\bar{n}} + \int_{\chi_0}^{\infty} d\chi \left[f(\chi) - \frac{\chi_0^{\bar{n}}}{\chi^{\bar{n}+1}} \right] \chi^{\bar{n}} + \chi_0^{\bar{n}} [H_{\bar{n}} - \gamma - \ln(\chi_0)] \right\}, \tag{A18}$$

where $\gamma \approx 0.5772$ is Euler's constant. After some algebra we obtain

$$l_2 = -\chi_0^{\bar{n}} \frac{2}{\bar{n}!} (-1)^{\bar{n}/2} \ln(C_{\bar{n}} \chi_0), \tag{A19}$$

where

$$C_{\bar{n}}[f(\chi)] = \exp\left\{ \gamma - H_{\bar{n}} - \int_0^{\chi_0} d\chi \, f(\chi) \left(\frac{\chi}{\chi_0}\right)^{\bar{n}} - \int_{\chi_0}^{\infty} d\chi \left[f(\chi) \left(\frac{\chi}{\chi_0}\right)^{\bar{n}} - \frac{1}{\chi} \right] \right\} \tag{A20}$$

is a finite constant, which provides the second and third lines of Eq. (A3). Plugging $\bar{n} = 2$ into Eq. (A20) results in Eq. (5).

APPENDIX B: LEADING BEHAVIOR OF $\hat{\psi}(u \to 0)$

We assume that $\psi(\tau)$ possesses the asymptotic behavior

$$\lim_{\tau \to \infty} \psi(\tau)\tau^{1+\nu} = \tau_0^{\nu}, \tag{B1}$$

where $\nu > 0$ and $\tau_0 > 0$ are real numbers. The Laplace transform of $\psi(\tau)$ is defined as

$$\hat{\psi}(u) = \int_0^{\infty} d\tau \, \psi(\tau)e^{-u\tau}. \tag{B2}$$

As we show below, given a positive integer $\bar{n}$, Eqs. (B1) and (B2) lead to

$$\hat{\psi}(u) \simeq \sum_{n=0}^{\bar{n}-1} \frac{(-u)^n}{n!}\langle \tau^n \rangle + \begin{cases} \Gamma(-\nu)(\tau_0 u)^{\nu}, & \bar{n}-1 < \nu < \bar{n} \\ \frac{1}{\bar{n}!}(-1)^{\bar{n}+1}(\tau_0 u)^{\bar{n}} \ln(C_{\bar{n}}\tau_0 u), & \nu = \bar{n}, \end{cases} \tag{B3}$$

where $C_{\bar{n}}[\psi(\tau)]$ is defined in the corresponding section. Using Eqs. (B1) and (B2), we extract all of the converging moments from the Laplace transform integral

$$\hat{\psi}(u) = \sum_{n=0}^{\bar{n}-1} \frac{(-u)^n}{n!}\langle \tau^n \rangle + \int_0^{\infty} d\tau \, \psi(\tau)\left[e^{-u\tau} - \sum_{n=0}^{\bar{n}-1} \frac{(-u\tau)^n}{n!}\right] \tag{B4}$$

and consider each of the cases in Eq. (B3) separately.

1. Noninteger ν

Let us assume that $\bar{n}-1 < \nu < \bar{n}$. In order to obtain the leading behavior of the second term of Eq. (B4), we consider the limit

$$l_0 = \lim_{u \to 0} \frac{1}{u^{\nu}} \int_0^{\infty} d\tau \, \psi(\tau)\left[e^{-u\tau} - \sum_{n=0}^{\bar{n}-1} \frac{(-u\tau)^n}{n!}\right]. \tag{B5}$$

Using l'Hôpital's rule $\bar{n}$ times yields

$$l_0 = \lim_{u \to 0} \frac{\Gamma(-\nu)u^{\bar{n}-\nu}}{\Gamma(-\nu+\bar{n})} \int_0^{\infty} d\tau \, \psi(\tau)\tau^{\bar{n}}e^{-u\tau}. \tag{B6}$$

Changing the integration variable to $\eta = u\tau$ produces

$$l_0 = \frac{\Gamma(-\nu)}{\Gamma(-\nu+\bar{n})} \lim_{u \to 0} \int_0^{\infty} d\eta \, \psi\left(\frac{\eta}{u}\right)\left(\frac{\eta}{u}\right)^{\nu+1}\eta^{\bar{n}-1-\nu}e^{-\eta}. \tag{B7}$$

We switch the order of the limit and integration, which together with the asymptotic behavior (B1) gives

$$l_0 = \frac{\tau_0^{\nu}\Gamma(-\nu)}{\Gamma(-\nu+\bar{n})} \int_{0^+}^{\infty} d\eta \, \eta^{\bar{n}-1-\nu}e^{-\eta} = \tau_0^{\nu}\Gamma(-\nu), \tag{B8}$$

which proves the first line of Eq. (B3).

2. Integer ν

Let us assume that $\nu = \bar{n}$, where $\bar{n}$ can be even or odd. In order to find the leading behavior of Eq. (B4), we consider the limit

$$l_1 = \lim_{u \to 0} \frac{1}{u^{\bar{n}} \ln(u)} \int_0^{\infty} d\tau \, \psi(\tau)\left[e^{-u\tau} - \sum_{n=0}^{\bar{n}-1} \frac{(-u\tau)^n}{n!}\right]. \tag{B9}$$

Using l'Hôpital's rule $\bar{n}+1$, we get

$$l_1 = \lim_{u \to 0}(-1)^{\bar{n}+1} \frac{u}{\bar{n}!} \int_0^{\infty} d\tau \, \psi(\tau)\tau^{\bar{n}+1}e^{-u\tau}. \tag{B10}$$

We change the integration variable to $\eta = u\tau$,

$$l_1 = \lim_{u \to 0} \frac{(-1)^{\bar{n}+1}}{\bar{n}!} \int_0^{\infty} d\eta \, \psi\left(\frac{\eta}{u}\right)\left(\frac{\eta}{u}\right)^{\bar{n}+1}e^{-\eta}, \tag{B11}$$

and switch the order of the limit and integration while applying the asymptotic behavior (B1),

$$l_1 = \frac{\tau_0^{\bar{n}}}{\bar{n}!}(-1)^{\bar{n}+1} \int_{0^+}^{\infty} d\eta \, e^{-\eta} = \frac{1}{\bar{n}!}(-1)^{\bar{n}+1}\tau_0^{\bar{n}}. \tag{B12}$$

To obtain the next-order correction, we evaluate the limit

$$l_2 = \lim_{u \to 0} \frac{1}{u^{\bar{n}}} \left\{ \int_0^\infty \psi(\tau) \left[e^{-u\tau} - \sum_{n=0}^{\bar{n}-1} \frac{(-u\tau)^n}{n!} \right] d\tau - \frac{\tau_0^{\bar{n}}}{\bar{n}!} (-1)^{\bar{n}+1} u^{\bar{n}} \ln(u) \right\}. \tag{B13}$$

We use l'Hôpital's rule $\bar{n}$ times to get

$$l_2 = \frac{(-1)^{\bar{n}}}{\bar{n}!} \lim_{u \to 0} \left\{ \int_0^\infty d\tau \, \psi(\tau) \tau^{\bar{n}} e^{-u\tau} + \tau_0^{\bar{n}} [\ln(u) + H_{\bar{n}}] \right\}. \tag{B14}$$

Splitting the integral at $\tau = \tau_0$ yields

$$l_2 = \frac{(-1)^{\bar{n}}}{\bar{n}!} \lim_{u \to 0} \left\{ \int_0^{\tau_0} d\tau \, \psi(\tau) \tau^{\bar{n}} e^{-u\tau} + \int_{\tau_0}^\infty d\tau \, \psi(\tau) \tau^{\bar{n}} e^{-u\tau} + \tau_0^{\bar{n}} [\ln(u) + H_{\bar{n}}] \right\}. \tag{B15}$$

We now add and subtract the term $\tau_0^{\bar{n}}/\tau^{\bar{n}+1}$ from $\psi(\tau)$ in the second integral in Eq. (B15),

$$l_2 = \frac{(-1)^{\bar{n}}}{\bar{n}!} \lim_{u \to 0} \left\{ \int_0^{\tau_0} d\tau \, \psi(\tau) \tau^{\bar{n}} e^{-u\tau} + \int_{\tau_0}^\infty d\tau \left[\psi(\tau) - \frac{\tau_0^{\bar{n}}}{\tau^{\bar{n}+1}} \right] \tau^{\bar{n}} e^{-u\tau} + \int_{\tau_0}^\infty d\tau \, \frac{\tau_0^{\bar{n}}}{\tau} e^{-u\tau} + \tau_0^{\bar{n}} [\ln(u) + H_{\bar{n}}] \right\}. \tag{B16}$$

Note that, due to the asymptotics (B1), the middle integral above is finite when $u \to 0$. The right integral in Eq. (B16) can be computed explicitly, after which the limit can be evaluated. Finally, we find

$$l_2 = \frac{1}{\bar{n}!} (-1)^{\bar{n}+1} \tau_0^{\bar{n}} \ln(C_{\bar{n}} \tau_0), \tag{B17}$$

where

$$C_{\bar{n}}[\psi(\tau)] = \exp \left\{ \gamma - H_{\bar{n}} - \int_0^{\tau_0} d\tau \, \psi(\tau) \left(\frac{\tau_0}{\tau} \right)^{\bar{n}} - \int_{\tau_0}^\infty d\tau \left[\psi(\tau) \left(\frac{\tau_0}{\tau} \right)^{\bar{n}} - \frac{1}{\tau} \right] \right\} \tag{B18}$$

is a finite constant, which concludes the second line of Eq. (B3). Plugging $\bar{n} = 2$ into Eq. (B18) results in Eq. (18).

APPENDIX C: ADDITIONAL STEPS IN THE DERIVATION OF LAMBERT SCALING FOR THE LÉVY WALK MODEL

Here we portray the additional steps which were omitted in Sec. III. Starting from Eq. (17), we expand $\hat{\psi}(u - i\boldsymbol{k} \cdot \boldsymbol{v})$ for small arguments

$$\hat{\psi}(u - i\boldsymbol{k} \cdot \boldsymbol{v}) \simeq 1 - \langle \tau \rangle (u - i\boldsymbol{k} \cdot \boldsymbol{v}) - \tfrac{1}{2} \tau_0^2 (u - i\boldsymbol{k} \cdot \boldsymbol{v})^2 \ln[C_\psi \tau_0 (u - i\boldsymbol{k} \cdot \boldsymbol{v})] \tag{C1}$$

and apply this expansion to the Montroll-Weiss equation (14),

$$\Pi_d(\boldsymbol{k}, u) \simeq \left\{ 1 + \left\langle \frac{\tau_0^2}{2\langle \tau \rangle} (u - i\boldsymbol{k} \cdot \boldsymbol{v}) \ln[C_\psi \tau_0 (u - i\boldsymbol{k} \cdot \boldsymbol{v})] \right\rangle \right\} \left\{ u + \left\langle \frac{\tau_0^2}{2\langle \tau \rangle} (u - i\boldsymbol{k} \cdot \boldsymbol{v})^2 \ln[C_\psi \tau_0 (u - i\boldsymbol{k} \cdot \boldsymbol{v})] \right\rangle \right\}^{-1}. \tag{C2}$$

We use the identity

$$\ln(a \pm ib) = \frac{1}{2} \ln(a^2 + b^2) \pm i \tan^{-1} \left(\frac{b}{a} \right) \tag{C3}$$

and the assumed symmetry of $F(\boldsymbol{v})$ in order to simplify Eq. (C2),

$$\begin{aligned} \Pi_d(\boldsymbol{k}, u) \simeq & \left\{ 1 + \frac{u\tau_0^2}{4\langle \tau \rangle} \langle \ln \{ C_\psi^2 \tau_0^2 [u^2 + (\boldsymbol{k} \cdot \boldsymbol{v})^2] \} \rangle - \frac{\tau_0^2}{2\langle \tau \rangle} \left\langle (\boldsymbol{k} \cdot \boldsymbol{v}) \tan^{-1} \left(\frac{\boldsymbol{k} \cdot \boldsymbol{v}}{u} \right) \right\rangle \right\} \\ & \times \left\{ u + \frac{u^2 \tau_0^2}{4\langle \tau \rangle} \langle \ln \{ C_\psi^2 \tau_0^2 [u^2 + (\boldsymbol{k} \cdot \boldsymbol{v})^2] \} \rangle - \frac{\tau_0^2}{4\langle \tau \rangle} \langle (\boldsymbol{k} \cdot \boldsymbol{v})^2 \ln \{ C_\psi^2 \tau_0^2 [u^2 + (\boldsymbol{k} \cdot \boldsymbol{v})^2] \} \rangle \right. \\ & \left. + \frac{u\tau_0^2}{\langle \tau \rangle} \left\langle (\boldsymbol{k} \cdot \boldsymbol{v}) \tan^{-1} \left(\frac{\boldsymbol{k} \cdot \boldsymbol{v}}{u} \right) \right\rangle \right\}^{-1}. \end{aligned} \tag{C4}$$

Using $\ln(1 + \epsilon^2) \simeq \epsilon^2$ and $\tan^{-1}(1/\epsilon) \simeq (\pi/2)\text{sgn}(\epsilon) - \epsilon$ for $\epsilon \to 0$, we discard irrelevant terms with respect to $\epsilon \sim u/kv$, so we have

$$\Pi_d(\boldsymbol{k}, u) \simeq \left\{ u - \frac{\tau_0^2}{4\langle \tau \rangle} \langle (\boldsymbol{k} \cdot \boldsymbol{v})^2 \ln [C_\psi^2 \tau_0^2 (\boldsymbol{k} \cdot \boldsymbol{v})^2] \rangle \right\}^{-1}. \tag{C5}$$

One may argue that this expansion breaks down when $v = 0$ or alternatively when $\boldsymbol{k} \cdot \boldsymbol{v} = 0$, but actually there is no problem. The former case is ruled out since our physical models have a positive constant for the speed $v = V = 1$ and as such we demand that

$F_d(v \neq 1) = 0$. The latter case is ruled out since $F_d(\boldsymbol{v})$ covers all velocity directions of the d-dimensional space, by construction. Therefore, it will always contain a part parallel to $\boldsymbol{k}$, regardless of $\boldsymbol{k}$'s direction. Returning to the time domain, we obtain

$$\tilde{P}_d(\boldsymbol{k}, t) \simeq \exp \left\{ \frac{t\tau_0^2}{4\langle\tau\rangle} \langle (\boldsymbol{k} \cdot \boldsymbol{v})^2 \ln \left[C_\psi^2 \tau_0^2 (\boldsymbol{k} \cdot \boldsymbol{v})^2 \right] \rangle \right\}. \quad (C6)$$

Substituting $\boldsymbol{\kappa} = \boldsymbol{k}\sqrt{\tau_0^2 \langle v^2 \rangle t \Omega_d(t)/4d\langle\tau\rangle}$, where $\Omega_d(t)$ is a scaling function, leads to

$$\tilde{P}_d(\boldsymbol{\kappa}, t) \simeq \left[\frac{4d\langle\tau\rangle}{\tau_0^2 \langle v^2 \rangle t \Omega_d(t)} \right]^{d/2} \exp \left\{ \frac{1}{\Omega_d(t)} \left\langle \frac{(\boldsymbol{\kappa} \cdot \boldsymbol{v})^2}{\langle v^2 \rangle/d} \ln \left[\frac{4dC_\psi^2 \langle\tau\rangle}{t\Omega_d(t)} \frac{(\boldsymbol{\kappa} \cdot \boldsymbol{v})^2}{\langle v^2 \rangle} \right] \right\rangle \right\}. \quad (C7)$$

We determine the slowly varying scaling function $\Omega_d(t)$ by demanding that $\ln[t\Omega_d(t)/4dC_\psi^2\langle\tau\rangle] = \Omega_d(t)$, obtaining Eq. (21). Thus, Eq. (C7) becomes

$$\tilde{P}_d(\boldsymbol{\kappa}, t) \simeq \left[\frac{2}{\xi_d(t)} \right]^d \exp \left[-\left\langle \frac{(\boldsymbol{\kappa} \cdot \boldsymbol{v})^2}{\langle v^2 \rangle/d} \right\rangle \right] \exp \left\{ \frac{1}{\Omega_d(t)} \left\langle \frac{(\boldsymbol{\kappa} \cdot \boldsymbol{v})^2}{\langle v^2 \rangle/d} \ln \left[\frac{(\boldsymbol{\kappa} \cdot \boldsymbol{v})^2}{\langle v^2 \rangle} \right] \right\rangle \right\}$$

$$\simeq \left[\frac{2}{\xi_d(t)} \right]^d \exp \left[-\left\langle \frac{(\boldsymbol{\kappa} \cdot \boldsymbol{v})^2}{\langle v^2 \rangle/d} \right\rangle \right] \left\{ 1 + \frac{1}{\Omega_d(t)} \left\langle \frac{(\boldsymbol{\kappa} \cdot \boldsymbol{v})^2}{\langle v^2 \rangle/d} \ln \left[\frac{(\boldsymbol{\kappa} \cdot \boldsymbol{v})^2}{\langle v^2 \rangle} \right] \right\rangle \right\}, \quad (C8)$$

where we expanded the exponential term in the second line due to the assumption of large t, which leads to large $\Omega_d(t)$. Equations (20) and (25) then follow from Eqs. (19) and (24), respectively, when combined with Eq. (C8).

APPENDIX D: DERIVATION OF THE INTEGRATION BOUNDARIES

1. Lorentz gas model

We denote by (x_0, y_0) the starting point on the (0,0) scatterer from which we assume the particle has originated. The pair $\{b, \beta\}$ and the trio $\{x_0, y_0, \beta\}$ are related by a simple transformation. To obtain it, we define the two vectors

$$\boldsymbol{R} = x_0\hat{x} + y_0\hat{y}, \quad \boldsymbol{B} = -b\sin(\beta)\hat{x} + b\cos(\beta)\hat{y}, \quad (D1)$$

where $\boldsymbol{B}$ can be seen as the red arrow in Fig. 6(a). Solving the equation $\boldsymbol{B} \cdot (\boldsymbol{R} - \boldsymbol{B}) = 0$ and $x_0(0, 0, R) = R$, we get the expressions

$$x_0(b, \beta, R) = \sqrt{R^2 - b^2} \cos(\beta) - b\sin(\beta),$$
$$y_0(b, \beta, R) = \sqrt{R^2 - b^2} \sin(\beta) + b\cos(\beta). \quad (D2)$$

By solving

$$[x_0(b, \beta, R) + \tau_{n,m}^*(b, \beta, R)\cos(\beta) - n]^2$$
$$+ [y_0(b, \beta, R) + \tau_{n,m}^*(b, \beta, R)\sin(\beta) - m]^2 = R^2, \quad (D3)$$

together with $\tau_{1,0}^*(0, 0, R) = 1 - 2R$, we obtain Eqs. (27) and (29). In order to extract the IBs of β and b from the inequalities (30)–(32), we notice that there are two classes of trajectories which reach the $(n, 1)$ scatterer, where $n \geqslant 0$. The first class's IBs are dictated by the origin and target scatterers. The second class's IBs are governed by the (1,0) and $(n - 1, 1)$ scatterers [this class does not exist for the (0,1) circle]. We split the β domain into two parts, which we label I and II, each corresponding to a class of trajectories, and denote the separator angle between them by $\beta_{n,1}^{\text{sep}}(R)$. Each of β's subdomains is associated with a different expression for b's IBs, which we denote by (i) and (ii). However, when $\beta = \beta_{n,1}^{\text{sep}}(R)$ the two expressions coincide. Therefore, $\beta_{n,1}^{\text{sep}}(R)$ can be found by comparing the lower (or upper) IB of (i) to that of (ii). Finding the top and bottom IBs of β relies on a similar idea, namely, using the expressions for b's IBs. When $\beta =$

$\beta_{n,1}^{\min}(R)$, the associated b subdomain (i) shrinks to zero. Thus, $\beta_{n,1}^{\min}(R)$ can be found by setting $b_{n,1}^{\min}(\beta, R) = b_{n,1}^{\max}(\beta, R)$ in the (i) expression. Identically, $\beta_{n,1}^{\max}(R)$ is found by setting $b_{n,1}^{\min}(\beta, R) = b_{n,1}^{\max}(\beta, R)$ in the (ii) expression. Starting with $n = 0$, the upper IB of β is set to $\pi/2$, which is possible due to symmetry. This is done in order to balance out the excess of distant-neighbor groups over nearest- and next-nearest-neighbor groups across the lattice, which is demonstrated in Fig. 7(a). Writing Eq. (30) in its explicit form, we get, for subdomain (i),

$$\cos(\beta) - R \leqslant b \leqslant \cos(\beta) + R. \quad (D4)$$

Since $\beta \leqslant \pi/2$ and $|b| \leqslant R$, the upper IB in Eq. (D4) is set to R. For β's lower IB, we equate b's IBs, $\cos(\beta) - R = R$, getting $\cos^{-1}(2R)$. Thus, we obtain, for $n = 0$,

$$\frac{\pi}{2} - \sin^{-1}(2R) \leqslant \beta \leqslant \frac{\pi}{2}, \quad \cos(\beta) - R \leqslant b \leqslant R. \quad (D5)$$

We continue with $n = 1$. Again, due to symmetry we can truncate β's upper IB to $\pi/4$. Equation (31) in its explicit form combined with $|b| \leqslant R$ then yields

$$\cos(\beta) - \sin(\beta) - R \leqslant b \leqslant R \quad \text{for (i)},$$
$$R - \sin(\beta) \leqslant b \leqslant \cos(\beta) - R \quad \text{for (ii)}. \quad (D6)$$

Here the β domain is sectioned into two parts, as said before: I, for which the (ii) inequality in Eq. (D6) is trivially fulfilled, and II, in which it needs to be upheld. Equating the IBs of (i) in Eq. (D6) yields the lower IB of β. We obtain

$$\frac{\pi}{4} - \sin^{-1}(\sqrt{2}R) \leqslant \beta \leqslant \frac{\pi}{4}. \quad (D7)$$

The separator angle between I and II can be found by comparing the lower (or upper) b IB of (i) to that of (ii), yielding $\beta = \cos^{-1}(2R)$. Therefore, we find, for $n = 1$,

$$\frac{\pi}{4} - \sin^{-1}(\sqrt{2}R) \leqslant \beta \leqslant \cos^{-1}(2R) \quad \text{for I},$$
$$\cos(\beta) - \sin(\beta) - R \leqslant b \leqslant R \quad \text{for (i)} \quad (D8)$$

and

$$\cos^{-1}(2R) \leqslant \beta \leqslant \frac{\pi}{4} \quad \text{for II},$$
$$R - \sin(\beta) \leqslant b \leqslant \cos(\beta) - R \quad \text{for (ii)}. \tag{D9}$$

Finally, Eq. (32), in its explicit form, provides

$$\cos(\beta) - n\sin(\beta) - R \leqslant b \leqslant R \quad \text{for (i)},$$
$$R - \sin(\beta) \leqslant b \leqslant \cos(\beta) - (n-1)\sin(\beta) - R \quad \text{for (ii)}, \tag{D10}$$

where we already implemented $|b| \leqslant R$ to (i)'s top IB. This time, there is no need to set the upper IB of β manually. For the bottom IB of β's subdomain I, one equates the IBs of (i) in Eq. (D10), namely, $\cos(\beta) - n\sin(\beta) = 2R$. By dividing this equality by $\sqrt{n^2 + 1}$ and using basic trigonometry, we have a general form of the lower IB of β [Eq. (33)]. The same is done for the upper IB of β's subdomain II, where (ii) of Eq. (D10) is used, yielding $\cos(\beta) - (n-2)\sin(\beta) = 2R$, which results in Eq. (34). The separator angle can be found by equating the top or bottom IBs of (i) to (ii), producing $\cos(\beta) - (n-1)\sin(\beta) = 2R$ and Eq. (36).

We finish this subsection with the case of $R = 0.3$, namely, four open corridors. As said in Sec. IV, the scatterer (2,1) is now shared by the horizontal and diagonal directions; thus we adjust its upper β IB. When β achieves its maximal value for the horizontal direction stripe, b's lower IB must be equal to $-R$. Thus we set $b_{2,1}^{\min}(\beta, R) = -R$ in Eq. (35) and obtain Eq. (39). Similarly to the horizontal case, there are two classes of trajectories to reach the $(m+1, m)$ scatterer. The first class's IBs are governed by the origin and target scatterers and the second class's IBs are dictated by the (1,1) and $(m, m-1)$ circles [this class does not exist for the (2,1) target scatterer]. Again, we split β's domain into two subdomains I and II; however, this time they switch places, i.e., the I part is of higher β values than the II part. Equation (40), in its explicit form, reads

$$-R \leqslant b \leqslant \cos(\beta) - 2\sin(\beta) + R \quad \text{for (i)}, \tag{D11}$$

where we set the lower b IB to $-R$ since $\beta \geqslant \sin^{-1}(2R)$ and $|b| \leqslant R$. For the upper IB of β we equate the IBs of b in Eq. (D11) to each other, namely, $-R = \cos(\beta) - 2\sin(\beta) + R$. Thus we obtain, for $m = 1$,

$$\sin^{-1}(2R) \leqslant \beta \leqslant \sin^{-1}\left(\frac{4R}{5} + \frac{1}{5}\sqrt{5 - 4R^2}\right). \tag{D12}$$

For $m > 1$, we write Eq. (41) in its explicit form

$$-R \leqslant b \leqslant m\cos(\beta) - (m+1)\sin(\beta) + R \quad \text{for (i)},$$
$$(m-1)\cos(\beta) - m\sin(\beta) + R \leqslant b \leqslant \cos(\beta)$$
$$- \sin(\beta) - R \quad \text{for (ii)}, \tag{D13}$$

where we set the bottom IB of (i) to $-R$, as before. The upper β IB is found by equating the top IB of (i) to $-R$ in Eq. (D13) and the bottom β IB is found by equating the top and bottom IBs of (ii) to each other. The separator angle is found in the same manner as for the horizontal case. Dividing the resulted expressions by $\sqrt{m^2 + (m+1)^2}$ and using basic trigonometry, we obtain Eqs. (42)–(45).

2. Stadium channel model

We denote by (x_0, y_0) the starting point on the (0,0) stadium from which we assume the particle has originated. The pair $\{a, \alpha\}$ and the trio $\{x_0, y_0, \alpha\}$ are related by a simple transformation. To obtain it, we define the two vectors

$$\boldsymbol{R} = x_0\hat{x} + y_0\hat{y}, \quad \boldsymbol{A} = -a\sin(\alpha)\hat{x} + a\cos(\alpha)\hat{y}, \tag{D14}$$

where $\boldsymbol{A}$ can be seen as the red arrow in Fig. 6(b). Solving the equation $\boldsymbol{A} \cdot (\boldsymbol{R} - \boldsymbol{A}) = 0$ and $y_0(0, 0) = -1$, we get the expressions

$$x_0(a, \alpha) = \sqrt{1 - a^2}\cos(\alpha) - a\sin(\alpha),$$
$$y_0(a, \alpha) = \sqrt{1 - a^2}\sin(\alpha) + a\cos(\alpha). \tag{D15}$$

By solving

$$[x_0(a, \alpha) + \tau_{2n,m}^*(a, \alpha)\cos(\alpha) - 2n]^2$$
$$+ [y_0(a, \alpha) + \tau_{2n,m}^*(a, \alpha)\sin(\alpha) - m]^2 = 1, \tag{D16}$$

together with $\tau_{0,0}^*(0, 0) = 2$, we obtain Eqs. (48) and (50). Simplifying Eq. (51) and using $-\pi/2 \leqslant \alpha \leqslant \pi/2$, we get Eq. (54). In order to extract α's lower IB from the inequalities (52), we notice that, as with the Lorentz gas model, when α hits its bottom IB, the a domain vanishes. Simplifying Eq. (52), we have

$$D\cos(\alpha) - \sin(\alpha) \leqslant a \leqslant \sin(\alpha), \tag{D17}$$

and thus we have $D\cos(\alpha) - \sin(\alpha) = \sin(\alpha)$ for α's lower IB, which is solved to obtain $\alpha_{0,D}^{\min} = \tan^{-1}(D/2)$. Finally, we notice that there are two classes of trajectories which reach the target stadiums of $n > 0$, as with the Lorentz gas case. The first class's IBs are dictated by the origin and target semicircles. The second class's IBs are governed by the origin and $(2n - 2, D)$ stadium walls [this class does not exist for the trajectories ending with the origin or $(0, D)$ semicircles]. We split the α domain into two parts, referred to as I and II, each corresponding to a class of trajectories, and denote the separator angle between them by $\alpha_{2n,D}^{\text{sep}}$. Each of α's subdomains is associated with a different expression for a's IBs, which we denote by (i) and (ii). However, when $\alpha = \alpha_{2n,D}^{\text{sep}}$ the two expressions coincide. Therefore, $\alpha_{2n,D}^{\text{sep}}$ can be found by comparing the lower (or upper) IB of (i) to that of (ii). Finding the top and bottom IBs of α relies on a similar idea, namely, using the expressions for a's IBs. When $\alpha = \alpha_{2n,D}^{\min}$, the associated a subdomain (i) shrinks to zero. Thus, $\alpha_{2n,D}^{\min}$ can be found by setting $a_{2n,D}^{\min}(\alpha) = a_{2n,D}^{\max}(\alpha)$ in the (i) expression. Identically, $\alpha_{2n,D}^{\max}$ is found by setting $a_{2n,D}^{\min}(\alpha) = a_{2n,D}^{\max}(\alpha)$ in the (ii) expression. Simplifying the first line of Eq. (53), we get

$$-\sin(\alpha) \leqslant a \leqslant \sin(\alpha), \quad D\cos(\alpha) - (2n+1)\sin(\alpha)$$
$$\leqslant a \leqslant D\cos(\alpha) - (2n-1)\sin(\alpha) \quad \text{for (i)}. \tag{D18}$$

This class of trajectories has its upper (lower) a IB dominated by the origin (target) stadium, and thus the top (bottom) IB for this class is taken from the first (second) inequality in Eq. (D18) such that

$$D\cos(\alpha) - (2n+1)\sin(\alpha) \leqslant a \leqslant \sin(\alpha) \quad \text{for (i)}. \tag{D19}$$

For the inequalities in the second line in Eq. (53) we get, after simplification,

$$-\sin(\alpha) \leqslant a \leqslant \sin(\alpha), \quad |a - D\cos(\alpha)$$
$$+ (2n-2)\sin(\alpha)| \geqslant \sin(\alpha) \quad \text{for (ii)}. \quad \text{(D20)}$$

This class of trajectories has its lower (upper) a IB dominated by the origin $[(2n-2, D)]$ stadium, and thus the bottom (top)

IB for this class is taken from the first (second) inequality in Eq. (D18) such that

$$-\sin(\alpha) \leqslant a \leqslant D\cos(\alpha) - (2n-1)\sin(\alpha) \quad \text{for (ii)}. \quad \text{(D21)}$$

Using the IBs of a in (i) and (ii) to extract the IBs of α in the way described above, we obtain Eqs. (55)–(58).

APPENDIX E: CALCULATIONS OF τ_0, $\langle\tau\rangle$, AND C_ψ

1. Lorentz gas model

Using Eq. (28) together with the integration boundaries (33)–(36), one can calculate $\psi(\tau)$ using a computational program like *Mathematica* and extract the constants τ_0, $\langle\tau\rangle$, and C_ψ from it. However, we found that an analytical expression for τ_0 can be calculated. It follows from its definition (1) that

$$\tau_0^2 = \lim_{T\to\infty} \frac{1}{T} \int_0^T d\tau \, \tau^3 \, \psi(\tau). \quad \text{(E1)}$$

Plugging Eq. (28) with two infinite corridors (i.e., $q = 0$) into Eq. (E1), we get

$$\tau_0^2 = 8 \lim_{T\to\infty} \frac{1}{T} \sum_{n=0}^{\infty} \int_{\beta_{n,1}^{\min}(R)}^{\beta_{n,1}^{\max}(R)} \frac{d\beta}{2\pi} \int_{b_{n,1}^{\min}(\beta,R)}^{b_{n,1}^{\max}(\beta,R)} \frac{db}{2R} \tau_{n,1}^{*3}(b,\beta,R) \theta[T - \tau_{n,1}^*(b,\beta,R)], \quad \text{(E2)}$$

where $\theta(\cdots)$ is the Heaviside step function and the factor of 8 arises from symmetry (see Fig. 7). Since $\tau_{n,m}^*(b,\beta,R)$ is the traveling distance to the (n,m) scatterer, it obeys $\tau_{n,1}^*(b,\beta,R) \simeq \sqrt{n^2 + (1-2R)^2} \simeq n$ when n is large; thus the Heaviside function truncates the sum in Eq. (E2) at $n = T$, and we have

$$\tau_0^2 = 8 \lim_{T\to\infty} \frac{1}{T} \sum_{n=0}^{T} \int_{\beta_{n,1}^{\min}(R)}^{\beta_{n,1}^{\max}(R)} \frac{d\beta}{2\pi} \int_{b_{n,1}^{\min}(\beta,R)}^{b_{n,1}^{\max}(\beta,R)} \frac{db}{2R} \tau_{n,1}^{*3}(b,\beta,R). \quad \text{(E3)}$$

Equation (E1) suggests that the integral over $\tau^3 \psi(\tau)$ grows linearly with T, and as such we expect that the sum in Eq. (E3) will behave similarly with T. We therefore write

$$\tau_0^2 = 8 \lim_{T\to\infty} \int_{\beta_{T,1}^{\min}(R)}^{\beta_{T,1}^{\max}(R)} \frac{d\beta}{2\pi} \int_{b_{T,1}^{\min}(\beta,R)}^{b_{T,1}^{\max}(\beta,R)} \frac{db}{2R} [\sqrt{T^2 + (1-2R)^2}]^3. \quad \text{(E4)}$$

Now the integrals can be easily performed. After evaluating the limit we get a closed expression for τ_0 [Eq. (37)]. The remaining constants $\langle\tau\rangle$ and C_ψ are defined via integrals over $\psi(\tau)$ rather than by a limit operation, and as such they cannot be obtained using end terms as we just did. Nevertheless, one is not required to calculate $\psi(\tau)$, but can use a simpler tactic. To calculate the mean time between collisions, we use its definition and plug into Eq. (28),

$$\langle\tau\rangle = 8 \sum_{n=0}^{\infty} \int_{\beta_{n,1}^{\min}(R)}^{\beta_{n,1}^{\max}(R)} \frac{d\beta}{2\pi} \int_{b_{n,1}^{\min}(\beta,R)}^{b_{n,1}^{\max}(\beta,R)} \frac{db}{2R} \tau_{n,1}^*(b,\beta,R). \quad \text{(E5)}$$

To achieve a designated precision, one can simply truncate the sum at a large enough T. For $T = 500$ we obtain $\langle\tau\rangle \approx 0.62155$. For C_ψ we find the following formula from Eq. (18):

$$C_\psi = \lim_{T\to\infty} \exp\left[\gamma - \frac{3}{2} + \ln\left(\frac{T}{\tau_0}\right) - \int_0^T d\tau \, \psi(\tau)\left(\frac{\tau}{\tau_0}\right)^2\right]. \quad \text{(E6)}$$

Plugging Eq. (28) into this expression and allowing the Heaviside function to truncate the sum at $n = T$ yields

$$C_\psi = \lim_{T\to\infty} \exp\left[\gamma - \frac{3}{2} + \ln\left(\frac{T}{\tau_0}\right) - 8 \sum_{n=0}^{T} \int_{\beta_{n,1}^{\min}(R)}^{\beta_{n,1}^{\max}(R)} \frac{d\beta}{2\pi} \int_{b_{n,1}^{\min}(\beta,R)}^{b_{n,1}^{\max}(\beta,R)} \frac{db}{2R} \frac{\tau_{n,1}^{*2}(b,\beta,R)}{\tau_0^2}\right]. \quad \text{(E7)}$$

This equation converges rather slowly due to the logarithmic term; hence we need to accelerate its convergence rate. To do that, we use the identity

$$\lim_{T\to\infty}\left[\ln(T) - \sum_{n=1}^{T} \frac{1}{n}\right] = -\gamma \quad \text{(E8)}$$

and write, taking the $n = 0$ summand out of the sum,

$$C_\psi = \lim_{T \to \infty} \exp \left\{ -\frac{3}{2} - \ln(\tau_0) - 8 \int_{\beta_{0,1}^{\min}(R)}^{\beta_{0,1}^{\max}(R)} \frac{d\beta}{2\pi} \int_{b_{0,1}^{\min}(\beta,R)}^{b_{0,1}^{\max}(\beta,R)} \frac{db}{2R} \frac{\tau_{0,1}^{*2}(b,\beta,R)}{\tau_0^2} \right.$$

$$\left. - \sum_{n=1}^{T} \left[8 \int_{\beta_{n,1}^{\min}(R)}^{\beta_{n,1}^{\max}(R)} \frac{d\beta}{2\pi} \int_{b_{n,1}^{\min}(\beta,R)}^{b_{n,1}^{\max}(\beta,R)} \frac{db}{2R} \frac{\tau_{n,1}^{*2}(b,\beta,R)}{\tau_0^2} - \frac{1}{n} \right] \right\}. \tag{E9}$$

We approximate $\tau_{n,1}^*(b, \beta, R)$ for large n as before and see, after performing the integrals, that the summands behave for $n \gg 1$ as

$$s_n \simeq 8 \int_{\beta_{n,1}^{\min}(R)}^{\beta_{n,1}^{\max}(R)} \frac{d\beta}{2\pi} \int_{b_{n,1}^{\min}(\beta,R)}^{b_{n,1}^{\max}(\beta,R)} \frac{db}{2R} \frac{n^2 + (1 - 2R)^2}{\tau_0^2} - \frac{1}{n} \simeq \frac{B_1}{n^2} + \frac{B_2}{n^3} + \frac{B_3}{n^4}, \tag{E10}$$

where B_1, B_2, and B_3 are some R-dependent coefficients. This behavior suggests that the partial sum S_T goes like

$$S_T = \sum_{n=1}^{T} s_n \simeq l_R + \frac{\tilde{B}_1}{T} + \frac{\tilde{B}_2}{T^2} + \frac{\tilde{B}_3}{T^3} \tag{E11}$$

for large T, where l_R is the desired limit. This implies that the Richardson extrapolation method can be used [see Eq. (8.1.16) in Ref. [34]]. For $T = 40$, we get $C_\psi \approx 4.4802 \times 10^{-4}$ by summing terms up to $n = T$ and extrapolating over the S_{37}, S_{38}, S_{39}, and S_{40} partial sums.

Extracting the needed constants for four open horizons, namely, $q > 0$, is done in a similar fashion, but this time we have $1/\sqrt{20} \leqslant R < 1/\sqrt{8}$. Plugging Eq. (28) into Eq. (E1) gives

$$\tau_0^2 = \frac{2}{\pi R}(1 - 2R)^2 + 8 \lim_{T \to \infty} \frac{1}{T} \sum_{m=1}^{\infty} \int_{\beta_{m+1,m}^{\min}(R)}^{\beta_{m+1,m}^{\max}(R)} \frac{d\beta}{2\pi} \int_{b_{m+1,m}^{\min}(\beta,R)}^{b_{m+1,m}^{\max}(\beta,R)} \frac{db}{2R} \tau_{m+1,m}^{*3}(b,\beta,R) \theta[T - \tau_{m+1,m}^*(b,\beta,R)]. \tag{E12}$$

Using geometrical considerations, this time we have $\tau_{m+1,m}^*(b, \beta, R) \simeq [2(m + 1/2)^2 + (1/\sqrt{2} - 2R)^2]^{1/2} \simeq \sqrt{2}m$ for large m, so the sum in Eq. (E12) is truncated at (the closest integer to) $T/\sqrt{2}$,

$$\tau_0^2 = \frac{2}{\pi R}(1 - 2R)^2 + \frac{8}{\sqrt{2}} \lim_{T \to \infty} \frac{\sqrt{2}}{T} \sum_{m=1}^{T/\sqrt{2}} \int_{\beta_{m+1,m}^{\min}(R)}^{\beta_{m+1,m}^{\max}(R)} \frac{d\beta}{2\pi} \int_{b_{m+1,m}^{\min}(\beta,R)}^{b_{m+1,m}^{\max}(\beta,R)} \frac{db}{2R} \tau_{m+1,m}^{*3}(b,\beta,R). \tag{E13}$$

After omitting the sum as was done for the case of two open horizons, Eq. (E13) becomes

$$\tau_0^2 = \frac{2}{\pi R}(1 - 2R)^2 + \frac{8}{\sqrt{2}} \lim_{T \to \infty} \int_{\beta_{T+1,T}^{\min}(R)}^{\beta_{T+1,T}^{\max}(R)} \frac{d\beta}{2\pi} \int_{b_{T+1,T}^{\min}(\beta,R)}^{b_{T+1,T}^{\max}(\beta,R)} \frac{db}{2R} \left[2\left(T + \frac{1}{2}\right)^2 + \left(\frac{1}{\sqrt{2}} - 2R\right)^2 \right]^{3/2}, \tag{E14}$$

which then yields Eq. (46). We are left with calculating the remaining parameters for the British flag case. For the mean time between collisions we have

$$\langle \tau \rangle = 8 \sum_{n=0}^{\infty} \int_{\beta_{n,1}^{\min}(R)}^{\beta_{n,1}^{\max}(R)} \frac{d\beta}{2\pi} \int_{b_{n,1}^{\min}(\beta,R)}^{b_{n,1}^{\max}(\beta,R)} \frac{db}{2R} \tau_{n,1}^*(b,\beta,R) + 8 \sum_{m=1}^{\infty} \int_{\beta_{m+1,m}^{\min}(R)}^{\beta_{m+1,m}^{\max}(R)} \frac{d\beta}{2\pi} \int_{b_{m+1,m}^{\min}(\beta,R)}^{b_{m+1,m}^{\max}(\beta,R)} \frac{db}{2R} \tau_{m+1,m}^*(b,\beta,R). \tag{E15}$$

Note that if one truncates the first sum in Eq. (E15) at T, one then needs to truncate the second sum at $T/\sqrt{2}$. Using $T = 500$, we obtain $\langle \tau \rangle \approx 1.1947$. For C_ψ we write

$$\ln(T) = (1 - q)\ln(T) + q\ln\left(\frac{T}{\sqrt{2}}\right) + \frac{1}{2}\ln(2)q \Rightarrow \lim_{T \to \infty} \left\{ \ln(T) - (1 - q)\sum_{n=1}^{T} \frac{1}{n} - q\sum_{m=1}^{T/\sqrt{2}} \frac{1}{m} \right\} = \frac{1}{2}\ln(2)q - \gamma, \tag{E16}$$

and consequently

$$C_\psi = \lim_{T \to \infty} \exp \left\{ \frac{1}{2}\ln(2)q - \frac{3}{2} - \ln(\tau_0) - 8 \int_{\beta_{0,1}^{\min}(R)}^{\beta_{0,1}^{\max}(R)} \frac{d\beta}{2\pi} \int_{b_{0,1}^{\min}(\beta,R)}^{b_{0,1}^{\max}(\beta,R)} \frac{db}{2R} \frac{\tau_{0,1}^{*2}(b,\beta,R)}{\tau_0^2} \right.$$

$$- \sum_{n=1}^{T} \left[8 \int_{\beta_{n,1}^{\min}(R)}^{\beta_{n,1}^{\max}(R)} \frac{d\beta}{2\pi} \int_{b_{n,1}^{\min}(\beta,R)}^{b_{n,1}^{\max}(\beta,R)} \frac{db}{2R} \frac{\tau_{n,1}^{*2}(b,\beta,R)}{\tau_0^2} - \frac{1 - q}{n} \right]$$

$$\left. - \sum_{m=1}^{T/\sqrt{2}} \left[8 \int_{\beta_{m+1,m}^{\min}(R)}^{\beta_{m+1,m}^{\max}(R)} \frac{d\beta}{2\pi} \int_{b_{m+1,m}^{\min}(\beta,R)}^{b_{m+1,m}^{\max}(\beta,R)} \frac{db}{2R} \frac{\tau_{m+1,m}^{*2}(b,\beta,R)}{\tau_0^2} - \frac{q}{m} \right] \right\}. \tag{E17}$$

The behavior displayed in Eq. (E11) was checked to be valid for both sums in Eq. (E17). Thus, we take $T = 40$ and use Richardson extrapolation for each sum separately by extrapolating over the last four partial sums (for the second sum we use terms for which $m \leqslant 28 \approx T/\sqrt{2}$), and obtain $C_\psi \approx 1.5250 \times 10^{-2}$.

2. Stadium channel model

We use an identical way as for the Lorentz gas to compute τ_0 analytically. Since $\tau^*_{2n,D}(a, \alpha)$ is the traveling distance to the *n*th upper semicircle, it is clear that $\tau^*_{2n,D}(a, \alpha) \simeq \sqrt{(2n+2)^2 + D^2}$ when n is large. Plugging Eq. (49) into Eq. (E1) and employing similar manipulations as before, we have

$$\tau_0^2 = 4 \lim_{T \to \infty} \frac{1}{T} \sum_{n=0}^{\infty} \int_{\alpha_{2n,D}^{\min}}^{\alpha_{2n,D}^{\max}} \frac{d\alpha}{2\pi} \int_{a_{2n,D}^{\min}(\alpha)}^{a_{2n,D}^{\max}(\alpha)} \frac{da}{2} \tau_{2n,D}^{*3}(a, \alpha) \theta[T - \tau^*_{2n,D}(a, \alpha)]. \tag{E18}$$

Since $\sqrt{(2n+2)^2 + D^2} \simeq 2n$ for large n, the Heaviside function truncates the sum in Eq. (E18) at $n = T/2$. Thus

$$\tau_0^2 = 2 \lim_{T \to \infty} \frac{2}{T} \sum_{n=0}^{T/2} \int_{\alpha_{2n,D}^{\min}}^{\alpha_{2n,D}^{\max}} \frac{d\alpha}{2\pi} \int_{a_{2n,D}^{\min}(\alpha)}^{a_{2n,D}^{\max}(\alpha)} \frac{da}{2} \tau_{2n,D}^{*3}(a, \alpha), \tag{E19}$$

and consequently

$$\tau_0^2 = 2 \lim_{T \to \infty} \int_{\alpha_{2T,D}^{\min}}^{\alpha_{2T,D}^{\max}} \frac{d\alpha}{2\pi} \int_{a_{2T,D}^{\min}(\alpha)}^{a_{2T,D}^{\max}(\alpha)} \frac{da}{2} [\sqrt{(2T+2)^2 + D^2}]^3. \tag{E20}$$

Now the integrals can be easily performed. After evaluating the limit we get a closed expression for τ_0 [Eq. (59)]. For the mean time between collisions we write

$$\langle \tau \rangle = 4 \int_{\alpha_{0,0}^{\min}}^{\alpha_{0,0}^{\max}} \frac{d\alpha}{2\pi} \int_{a_{0,0}^{\min}(\alpha)}^{a_{0,0}^{\max}(\alpha)} \frac{da}{2} \tau_{0,0}^*(a, \alpha) + 4 \sum_{n=0}^{\infty} \int_{\alpha_{2n,D}^{\min}}^{\alpha_{2n,D}^{\max}} \frac{d\alpha}{2\pi} \int_{a_{2n,D}^{\min}(\alpha)}^{a_{2n,D}^{\max}(\alpha)} \frac{da}{2} \tau_{2n,D}^*(a, \alpha). \tag{E21}$$

We truncate the sum at $T = 500$, and obtain $\langle \tau \rangle \approx 2.57016$. For C_ψ we have

$$C_\psi = \lim_{T \to \infty} \exp \left\{ \ln \left(\frac{2}{\tau_0} \right) - \frac{3}{2} - 4 \int_{\alpha_{0,0}^{\min}}^{\alpha_{0,0}^{\max}} \frac{d\alpha}{2\pi} \int_{a_{0,0}^{\min}(\alpha)}^{a_{0,0}^{\max}(\alpha)} \frac{da}{2} \frac{\tau_{0,0}^{*2}(a, \alpha)}{\tau_0^2} - 4 \int_{\alpha_{0,D}^{\min}}^{\alpha_{0,D}^{\max}} \frac{d\alpha}{2\pi} \int_{a_{0,D}^{\min}(\alpha)}^{a_{0,D}^{\max}(\alpha)} \frac{da}{2} \frac{\tau_{0,D}^{*2}(a, \alpha)}{\tau_0^2} \right.$$
$$\left. - \sum_{n=1}^{T/2} \left[4 \int_{\alpha_{2n,D}^{\min}}^{\alpha_{2n,D}^{\max}} \frac{d\alpha}{2\pi} \int_{a_{2n,D}^{\min}(\alpha)}^{a_{2n,D}^{\max}(\alpha)} \frac{da}{2} \frac{\tau_{2n,D}^{*2}(a, \alpha)}{\tau_0^2} - \frac{1}{n} \right] \right\}. \tag{E22}$$

Substituting $\tau_{2n,D}^*(a, \alpha) \simeq \sqrt{(2n+2)^2 + D^2}$ for $n \gg 1$ and evaluating the integrals, we observe the behavior

$$s_n \simeq 4 \int_{\alpha_{2n,D}^{\min}}^{\alpha_{2n,D}^{\max}} \frac{d\alpha}{2\pi} \int_{a_{2n,D}^{\min}(\alpha)}^{a_{2n,D}^{\max}(\alpha)} \frac{da}{2} \frac{(2n+2)^2 + D^2}{\tau_0^2} - \frac{1}{n} \simeq \frac{A_1}{n^2} + \frac{A_2}{n^3} + \frac{A_3}{n^4}, \tag{E23}$$

where A_1, A_2, and A_3 are some *D*-dependent coefficients. This behavior suggests that the partial sum S_T goes like

$$S_T = \sum_{n=1}^{T} s_n \simeq l_D + \frac{\tilde{A}_1}{T} + \frac{\tilde{A}_2}{T^2} + \frac{\tilde{A}_3}{T^3} \tag{E24}$$

for large T, where l_D is the desired limit. Once again, we employ the Richardson extrapolation method. For $T = 60$, we get $C_\psi \approx 1.0903 \times 10^{-5}$ by summing terms up to $n = T/2$ and extrapolating over the S_{27}, S_{28}, S_{29}, and S_{30} partial sums.

---

[1] H. A. Lorentz, Proc. Roy. Acad. Amst. **7**, 438 (1905).

[2] J. P. Bouchaud and P. Le Doussal, J. Stat. Phys. **41**, 225 (1985).

[3] M. Courbage, M. Edelman, S. M. S. Fathi, and G. M. Zaslavsky, Phys. Rev. E **77**, 036203 (2008).

[4] G. Cristadoro, T. Gilbert, M. Lenci, and D. P. Sanders, Phys. Rev. E **90**, 050102(R) (2014).

[5] G. Cristadoro, T. Gilbert, M. Lenci, and D. P. Sanders, Phys. Rev. E **90**, 022106 (2014).

[6] R. M. Feliczaki, E. Vicentini, and P. P. González-Borrero, Phys. Rev. E **96**, 052117 (2017).

[7] R. Klages, S. S. G. Gallegos, J. Solanpää, M. Sarvilahti, and E. Räsänen, Phys. Rev. Lett. **122**, 064102 (2019).

[8] J. Vollmer, L. Rondoni, M. Tayyab, C. Giberti, and C. Mejía-Monasterio, arXiv:1903.12500.

[9] L. A. Bunimovich, Commun. Math. Phys. **65**, 295 (1979).

[10] C. Boldrighini, L. A. Bunimovich, and Y. G. Sinai, J. Stat. Phys. **32**, 477 (1983).

[11] L. A. Bunimovich, Zh. Éksp. Teor. Fiz. **89**, 1452 (1985) [Sov. Phys. JETP **62**, 842 (1985)].

[12] P. M. Bleher, J. Stat. Phys. **66**, 315 (1992).

[13] P. Dahlqvist, Nonlinearity **10**, 159 (1997).

[14] D. Szász and T. Varjú, J. Stat. Phys. **129**, 59 (2007).

[15] F. P. Boca and A. Zaharescu, Commun. Math. Phys. **269**, 425 (2007).

[16] N. Chernov, J. Stat. Phys. **127**, 21 (2007).

[17] N. Chernov and H. K. Zhang, Commun. Math. Phys. **277**, 305 (2008).

[18] D. I. Dolgopyat and N. L. Chernov, Russ. Math. Surv. **64**, 651 (2009).

[19] J. Marklof and A. Strömbergsson, Geom. Funct. Anal. **21**, 560 (2011).

[20] C. P. Dettmann, J. Stat. Phys. **146**, 181 (2012).

[21] C. P. Dettmann, Commun. Theor. Phys. **62**, 521 (2014).

[22] J. Marklof and B. Tóth, Commun. Math. Phys. **347**, 933 (2016).

[23] L. Zarfaty, A. Peletskyi, I. Fouxon, S. Denisov, and E. Barkai, Phys. Rev. E **98**, 010101(R) (2018).

[24] M. F. Shlesinger, B. J. West, and J. Klafter, Phys. Rev. Lett. **58**, 1100 (1987).

[25] V. Zaburdaev, S. Denisov, and J. Klafter, Rev. Mod. Phys. **87**, 483 (2015).

[26] V. Zaburdaev, I. Fouxon, S. Denisov, and E. Barkai, Phys. Rev. Lett. **117**, 270601 (2016).

[27] I. Fouxon, S. Denisov, V. Zaburdaev, and E. Barkai, J. Phys. A: Math. Theor. **50**, 154002 (2017).

[28] C. Börgers and C. Greengard, C. R. Math. **356**, 679 (2018).

[29] Refer to http://functions.wolfram.com for more information.

[30] B. V. Gnedenko and A. N. Kolmogorov, *Limit Distributions for Sums of Independent Random Variables* (Addison-Wesley, Cambridge, 1968).

[31] E. W. Montroll and G. H. Weiss, J. Math. Phys. **6**, 167 (1965).

[32] A. Rebenshtok, S. Denisov, P. Hänggi, and E. Barkai, Phys. Rev. Lett. **112**, 110601 (2014).

[33] I. Fouxon and P. Ditlevsen, arXiv:1908.03094.

[34] C. M. Bender and S. A. Orszag, *Advanced Mathematical Methods for Scientists and Engineers* (McGraw-Hill, New York, 1978).